

Cite this: *Chem. Sci.*, 2024, 15, 6583

All publication charges for this article have been paid for by the Royal Society of Chemistry

Fine-regulation of gradient gate-opening in nanoporous crystals for sieving separation of ternary C3 hydrocarbons†

Shuang Liu,^{‡a} Yuhang Huang,^{‡b} Jingmeng Wan,^b Jia-Jia Zheng,^c Rajamani Krishna,^{id d} Yi Li,^b Kai Ge,^{*b} Jie Tang^b and Jingui Duan^{id *b}

The adsorptive separation of ternary propyne (C₃H₄)/propylene (C₃H₆)/propane (C₃H₈) mixtures is of significant importance due to its energy efficiency. However, achieving this process using an adsorbent has not yet been accomplished. To tackle such a challenge, herein, we present a novel approach of fine-regulation of the gradient of gate-opening in soft nanoporous crystals. Through node substitution, an exclusive gate-opening to C₃H₄ (17.1 kPa) in NTU-65-FeZr has been tailored into a sequential response of C₃H₄ (1.6 kPa), C₃H₆ (19.4 kPa), and finally C₃H₈ (57.2 kPa) in NTU-65-CoTi, of which the gradient framework changes have been validated by *in situ* powder X-ray diffractions and modeling calculations. Such a significant breakthrough enables NTU-65-CoTi to sieve the ternary mixtures of C₃H₄/C₃H₆/C₃H₈ under ambient conditions, particularly, highly pure C₃H₈ (99.9%) and C₃H₆ (99.5%) can be obtained from the vacuum PSA scheme. In addition, the fully reversible structural change ensures no loss in performance during the cycling dynamic separations. Moving forward, regulating gradient gate-opening can be conveniently extended to other families of soft nanoporous crystals, making it a powerful tool to optimize these materials for more complex applications.

Received 16th October 2023

Accepted 17th March 2024

DOI: 10.1039/d3sc05489f

rsc.li/chemical-science

Introduction

Efficient separation of the ternary C3 hydrocarbons is crucial for the petrochemical industry as C₃H₆ is an essential feedstock for valuable commodities.¹ Currently, the separation process involves energy-intensive catalytic hydrogenation and cryogenic distillation, which accounts for nearly 3% of all separation energy.^{1–3} Therefore, there is a need for a more energy-efficient technology for this task. Adsorption separation using porous materials, specifically porous coordination polymers (PCPs), shows great promise due to their finely designed pore chemistry.^{4–13} In this regard, recent progress has been made in binary separations using strategies such as π -complexation,

sieving strategies and kinetic diffusion.^{14–23} However, the similar molecular sizes and kinetic diameters exacerbate the challenge of C₃H₄/C₃H₆/C₃H₈ separation, particularly by one material.

Recent research has shown that the purification of ethylene from a complex mixture of C2 hydrocarbons and carbon dioxide can be achieved using sequentially packed sorbents, where the three impurities were captured by three PCPs.²⁴ Although this strategy requires overcoming the difficulties of preparation of the three materials, and also their rational packing, it enables us to believe that integrating gradient sorbent–sorbate interactions may address the challenge of C₃H₄/C₃H₆/C₃H₈ separation in a single domain, as well as the precise understanding of hierarchical sites or gradient gate-openings.

The concept of hierarchical sites holds certain theoretical feasibility, but its implementation is hindered by the significant limitations in rational assembly of these sites in a confined nanospace. Comparably, the strategy of gradient gate-openings shows promising prospects. Since the early reports of soft crystals,^{25,26} the soft nature of these materials has been gradually understood, that is, the stronger the interaction, the earlier the gate-opening.^{27,28} In addition, soft frameworks can exhibit sensitive responses to even extremely small stimuli.^{29–31} Given these advantages, significant efforts have been dedicated to the construction of soft PCPs;^{27,29,32–35} however, neither the fine pre-design nor function-oriented synthesis of such a material,

^aHenan Engineering Research Center for Green Synthesis of Pharmaceuticals, College of Chemistry and Chemical Engineering, Shangqiu Normal University, Shangqiu 476000, China

^bState Key Laboratory of Materials-Oriented Chemical Engineering, College of Chemical Engineering, Nanjing Tech University, Nanjing 211816, China. E-mail: gekai@njtech.edu.cn; duanjingui@njtech.edu.cn

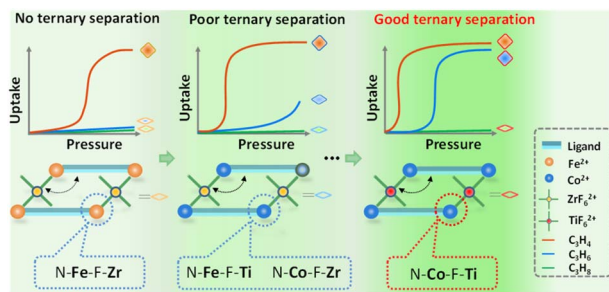
^cLaboratory of Theoretical and Computational Nanoscience, National Center for Nanoscience and Technology, Chinese Academy of Sciences, Beijing 100190, China

^dVan't Hoff Institute for Molecular Sciences, University of Amsterdam, Science Park 904, 1098 XH Amsterdam, The Netherlands

† Electronic supplementary information (ESI) available. CCDC 2284815–2284818. For ESI and crystallographic data in CIF or other electronic format see DOI: <https://doi.org/10.1039/d3sc05489f>

‡ These authors contributed equally to this work.





Scheme 1 Illustration of fine-regulation of gradient gate-opening in soft NTU-65-series via node substitution for sieving separation of C₃ hydrocarbons in a single domain.

whose framework can sequentially recognize these similar molecules, has yet been reported.

During our investigation of porous materials,^{20,36,37} we have reported a soft crystal, NTU-65, [Cu(L)₂(SiF₆)] (L = 1,4-di(1H-imidazolyl)benzene). The temperature dependent gate-opening allows it to show a sieving separation of C₂H₄/C₂H₂/CO₂ mixtures.

However, this framework cannot separate the equimolar C₃H₆/C₃H₈ due to a small difference in uptake at this ratio caused by the gate-opening effect which either occurs too early or too late (Fig. S2†). Inspired by reticular chemistry³⁸ and NTU-65, herein, we report a fine tuning of the framework softness via node substitution in a series of PCPs (NTU-65-series: NTU-65-FeZr, NTU-65-FeTi, NTU-65-CoZr and NTU-65-CoTi, Scheme 1), as the metal nodes may alter the transformation characteristics of soft structures. As expected, a sole gate-opening toward C₃H₄ in NTU-65-FeZr evolves into a gradient response to C₃H₄ and C₃H₆ in NTU-65-CoTi, yielding an unprecedented breakthrough of sieving separation of C₃H₄/C₃H₆/C₃H₈.

Results and discussion

Solvothermal reactions of L and the corresponding metal salt provide NTU-65-series (Fig. S3†). They crystallize in the monoclinic system (Table S1†) and adopt the same coordination configurations. The M1 centres (M1: Fe²⁺ or Co²⁺) of NTU-65-series are connected by four imidazole N atoms in a planar configuration from four L and two F atoms in the axial vertex from two M₂F₆²⁻ (M₂: Zr⁴⁺ or Ti⁴⁺) ions. As a result, cross-linked 2D channels are observed in the packed frameworks, although the window apertures undergo minimal changes (Fig. 1a, b and S4–S8†), along with similar accessible volumes (43.5%, 44.8%, 42.4% and 44.8%).³⁹ To reach the adjacent nodes, the dihedral angle between the benzene and imidazole rings in L in NTU-65-series shows significant changes. For example, the angle of the L_{Cis} in NTU-65-FeZr is as large as 14.81°, while this angle decreases to 3.45° in NTU-65-FeTi (Fig. 1c). Additionally, the dihedral angle in L_{Trans} in NTU-65-CoTi is up to 22.69°. Therefore, different degrees of softness are expected in the NTU-65-series. Phase purity of the four crystals has been confirmed by X-ray powder diffraction measurement (Fig. S9†). In addition, all samples are thermally stable, up to 350 °C (Fig. S10†).

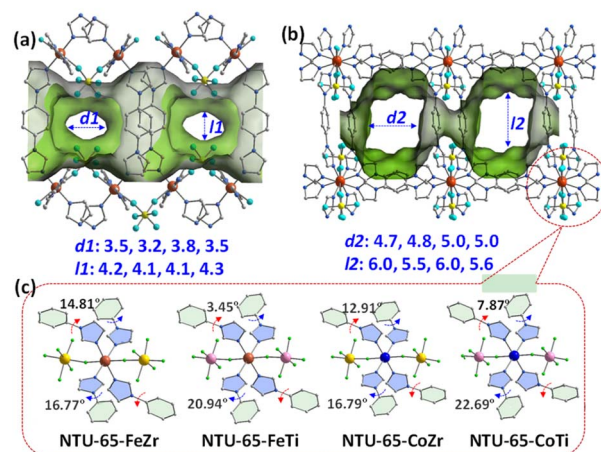


Fig. 1 Crystal structure of NTU-65-series along the *a*-axis (a) and *b*-axis (b). Comparison of the dihedral angle in L in NTU-65 series (c).

Permanent porosity of the activated NTU-65-series was evaluated using N₂ adsorption measurements at 77 K (Fig. S12†). Initially, all samples show minimal N₂ uptake until reaching $P/P_0 = 0.61, 0.26, 0.27$ and 0.24 . However, a peculiar ‘kink’ phenomenon occurred in all of them. This is due to the rapid increase in adsorption capacity of the crystals after instantaneous gate-opening under this condition, accompanied by a rapid decrease in system pressure, to $P/P_0 = 0.10, 0.07, 0.05$ and 0.04 , respectively. Subsequently, N₂ uptake increases with increased pressure in NTU-65-FeZr, while type-I adsorption isotherms were observed in NTU-65-FeTi and NTU-65-CoTi. Differently, NTU-65-CoZr exhibits a second adsorption platform before reaching $P/P_0 = 0.6$, followed by pressure-dependent uptake. Despite these differences, all four crystals demonstrated a similar maximum N₂ capacity (219.5 to 236.2 cm³ g⁻¹). Evaluated by using these isotherms, the crystals exhibit comparable surface areas (540–610 m² g⁻¹) and pore volumes (0.34–0.36 cm³ g⁻¹) (Fig. S13, S14 and Table S2†). Additionally, all isotherms display desorption hysteresis, confirming the filling effect of the soft frameworks.^{40,41}

To further investigate structural softness, CO₂ isotherms were collected at 195 K, as CO₂ may interact differently with the frameworks compared to N₂.^{42,43} Unlike the ‘kink’ phenomenon in the above N₂ isotherms, all CO₂ uptakes of the NTU-65-series increase with elevated pressure. Meanwhile, gradient adsorption platforms indicating sequential gate-openings were clearly observed in NTU-65-series. For NTU-65-FeZr, the first gate-opening occurs at 2.1 kPa, followed by the second and third gate-opening at 22.8 and 56.3 kPa, respectively (Fig. 2a). However, NTU-65-FeTi shows an earlier first gate-opening pressure (OP) of 1.7 kPa. The second and third gate-openings in NTU-65-FeZr merge into one in NTU-65-FeTi, at 31.4 kPa (Fig. 2b). Notably, three gate-openings appear again in NTU-65-CoZr (starting at 0.8, 14.6 and 45.8 kPa), whose responsive pressures are all lower than that of NTU-65-FeZr, and the first OP is also lower than that of NTU-65-FeTi (Fig. 2c). Remarkably, NTU-65-CoTi exhibits an advancement of the first OP at 0.5 kPa, followed by a second quick uptake at 18.8 kPa (Fig. 2d). Therefore, these isotherms



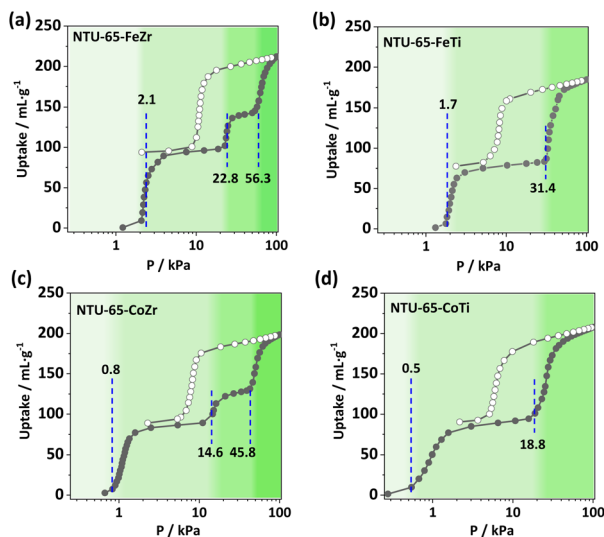


Fig. 2 CO₂ adsorption isotherms of NTU-65-series (a)–(d) at 195 K.

indicate that the four activated crystals possess non-porous characteristics and can be opened by N₂ or CO₂ once the stimuli exceed the energy barrier controlling the framework closure. Meanwhile, the gradually decreased pressure (2.1 to 0.5 kPa) for the first gate-opening reflects the fact that the four frameworks show different sensitivities to external stimuli. Additionally, the difference in multi-step gate-openings in them validates the effectiveness of the node substitution strategy in regulation of the framework with gradient softness, which may provide a promising platform for sequential recognition of gases with extremely small differences.

To investigate the function of gradient and sensitive gate-openings, adsorption isotherms of C₃H₄, C₃H₆ and C₃H₈ were collected on NTU-65-series (Fig. 3 and S15–S18†). NTU-65-FeZr

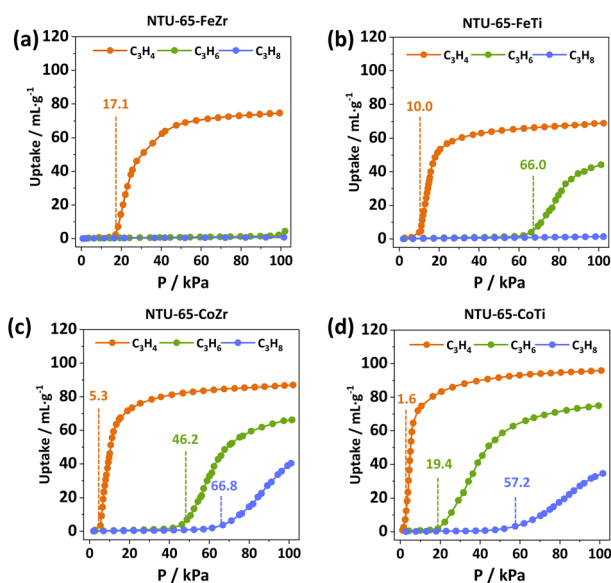


Fig. 3 C₃H₄, C₃H₆ and C₃H₈ adsorption isotherms of NTU-65-series (a)–(d) at 273 K.

exhibits minimal uptake of C₃H₆ and C₃H₈ at the threshold pressure, whereas C₃H₄ adsorption begins at 17.1 kPa with a maximum capacity of 74.7 cm³ g⁻¹ (Fig. 3a). Meanwhile, the starting OP is advanced to 10.0 kPa in NTU-65-FeTi, along with nearly the same C₃H₄ capacity (69.0 cm³ g⁻¹) (Fig. 3b). Unlike NTU-65-FeZr, C₃H₆ molecules open the framework of NTU-65-FeTi at 66.0 kPa with a capacity of 44.2 cm³ g⁻¹ at 100 kPa (Fig. 3c). Interestingly, the OP of the three gases (C₃H₄: 5.3 kPa, C₃H₆: 46.2 kPa and C₃H₈: 66.8 kPa) exhibit a forward movement again in NTU-65-CoZr (Fig. 3d). However, the isotherms indicate two crucial issues that may arise during the dynamic separation of such ternary mixtures: (1) insufficient partial pressure for C₃H₄ adsorption (far larger than 1 kPa); and (2) lower separation performance between C₃H₆ and C₃H₈ (small uptake difference of only 7.6 cm³ g⁻¹ at around 50 kPa). Remarkably, these issues may be solved by using NTU-65-CoTi, which exhibits rapid uptake of C₃H₄ at 1.6 kPa and a significantly improved uptake difference between C₃H₆ and C₃H₈, reaching as high as 55.9 cm³ g⁻¹ at 50 kPa. Additionally, the total C₃H₄ capacity is increased to 95.9 cm³ g⁻¹. Moreover, the uptake ratios of binary mixtures (C₃H₄/C₃H₆, C₃H₆/C₃H₈ and C₃H₄/C₃H₈) were significantly and simultaneously improved compared to that of other benchmark materials (Table 1 and S3†).

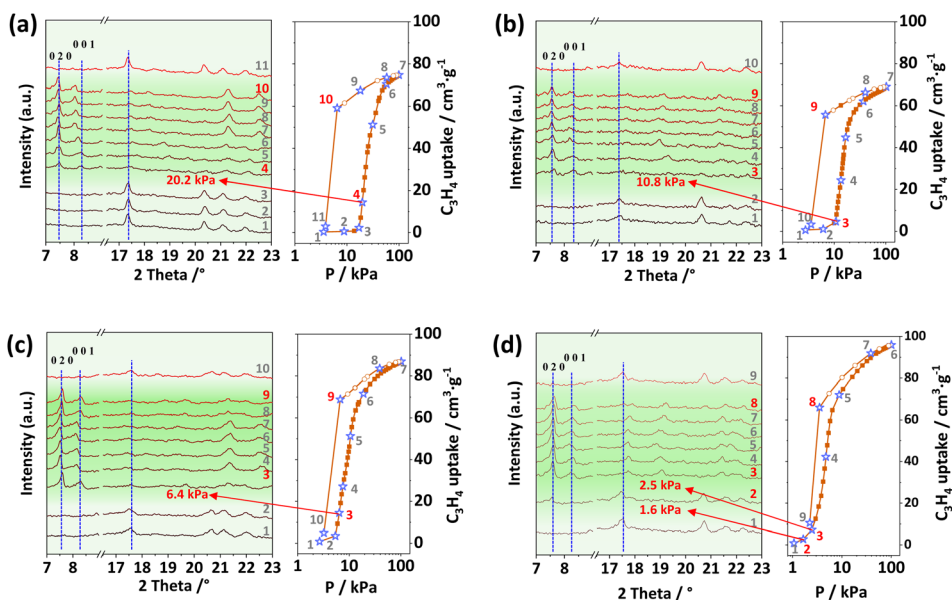
To confirm the systemic structural changes, *in situ* powder X-ray diffraction patterns/sorption measurements were performed (Fig. 4). The characteristic peaks corresponding to crystal faces of [0 2 0] and [0 0 1] in the as-synthesized phases (at about 6.5 and 7.2°) become weaker and shift to a higher-angle region in the activated crystals, indicative of structural contraction commonly observed in flexible PCPs. However, these two peaks reappear at similar positions to those obtained from their as-synthesized phases after an increase in pressure. Additionally, these open structures transform back into the closed state when the pressure decreases to a very low value, showing reversible sorption and structural changes in NTU-65-series. In addition, gas-loaded crystallographic analysis has also been attempted to explore the detailed structural changes. However, the small crystal size and crack after activation results in extremely weak or no diffraction. To understand the trend in softness of these PCPs, we conducted density functional theory (DFT) calculations taking C₃H₄ as the probe molecule (Fig. S20†). Previously, we have shown that the gate-opening pressure of PCPs induced by gas adsorption is dependent on the binding energy of the gas molecule with the PCP.⁴⁴ We therefore calculated the binding energies of C₃H₄ with the NTU-65-series. The binding energy increases (becomes more negative) in the following order: NTU-65-FeZr (-7.8 kcal mol⁻¹) < NTU-65-FeTi (-8.1 kcal mol⁻¹) < NTU-65-CoZr (-8.5 kcal mol⁻¹) < NTU-65-CoTi (-9.1 kcal mol⁻¹). This is consistent with the order of gate-opening pressure of these PCPs in response to C₃H₄ adsorption for these PCPs (Fig. 3).

The sequential recognition of C3 hydrocarbons encouraged us to perform dynamic separations. Given the commonly encountered ratio of C3 hydrocarbons in industry, a simulated feed-gas of C₃H₄/C₃H₆/C₃H₈ (0.5/49.75/49.75, v/v/v) was used for breakthrough experiments at 273 K. Consistent with the single-component gas isotherms, C₃H₆ and C₃H₈ elute simultaneously



Table 1 Summarized capacities ($\text{cm}^3 \text{g}^{-1}$) and uptake ratios of C3 hydrocarbons for NTU-65-series at 273 K

PCPs	C_3H_4	C_3H_6	C_3H_8	Uptake ratios		
	0.1 bar	0.5 bar	0.5 bar	$\text{C}_3\text{H}_4/\text{C}_3\text{H}_6$ (0.1/0.5)	$\text{C}_3\text{H}_6/\text{C}_3\text{H}_8$ (0.5/0.5)	$\text{C}_3\text{H}_4/\text{C}_3\text{H}_8$ (0.1/0.5)
NTU-65-CoTi	73.93	57.44	1.55	1.28	37.05	47.70
NTU-65-CoZr	46.24	8.55	0.96	5.41	8.91	48.17
NTU-65-FeTi	3.93	1.27	0.73	3.01	1.74	5.34
NTU-65-FeZr	0.59	0.74	0.51	0.80	1.45	1.16

Fig. 4 *In situ* PXRD patterns of NTU-65-FeZr (a), NTU-65-FeTi (b), NTU-65-CoZr (c) and NTU-65-CoTi (d) during C_3H_4 adsorption/desorption at 273 K.

from the NTU-65-FeZr sample bed, while C_3H_4 was captured until 85.8 min g^{-1} , showing impossible ternary separation (Fig. 5a). For NTU-65-CoZr, C_3H_8 was detected as the first elution at 19.3 min g^{-1} , followed by C_3H_6 at 27.8 min g^{-1} . Additionally, C_3H_4 passes through the column at 106.3 min g^{-1} (Fig. 5b). Considering the OP of C_3H_6 (46.2 kPa) and the small uptake difference ($7.6 \text{ cm}^3 \text{ g}^{-1}$) of $\text{C}_3\text{H}_6/\text{C}_3\text{H}_8$ in NTU-65-CoZr, the observable separation time of $\text{C}_3\text{H}_6/\text{C}_3\text{H}_8$ should be attributed to the slight pore opening, caused by accumulated C_3H_6 adsorption. This phenomenon is similar to the selective C_3H_4 or C_2H_2 capture in GeFSIX-dps-Zn⁴⁵ and Co(4-DPDS)₂MoO₄,⁴⁶ respectively, where the partial pressures of C_3H_4 (10 kPa) or C_2H_2 (1 kPa) in the feed-gas for breakthrough separations are lower than that of the corresponding OPs ($\sim 16 \text{ kPa}$ and $\sim 17 \text{ kPa}$) of the frameworks at the same temperature. In addition, a similar and insufficient ternary separation was also observed in NTU-65-FeTi. Remarkably, NTU-65-CoTi exhibits a significant separation of the ternary mixture of $\text{C}_3\text{H}_4/\text{C}_3\text{H}_6/\text{C}_3\text{H}_8$, in which highly pure C_3H_8 elutes out at 17.0 min g^{-1} , while the outflows of C_3H_6 and C_3H_4 from the sample bed are around 41.1 min g^{-1} and 132.9 min g^{-1} (Fig. 5c). Additionally, the further extended retention time of C_3H_4 (from 85.8 min g^{-1} in NTU-65-FeZr to 132.9 min g^{-1} in NTU-65-CoTi) reflects the increased

cumulative effect in NTU-65-series, as structural deformation becomes easier. To the best of our knowledge, the PCPs, including rigid and soft frameworks, have been widely explored for gas separations; however, this is the first example that can separate C3 hydrocarbons in one-step in a single domain. Furthermore, this promising separation was also confirmed at increased velocity (5 and 10 mL min^{-1}) of such ternary mixtures, as well as the binary mixtures (Fig. S21–S27 and Tables S4–S7†). More importantly, due to the reversible structural changes, there is almost no performance loss during the cycling measurements on NTU-65-CoTi (Fig. 5d and S28†), a critical factor in evaluating the feasibility of the adsorbents.

Based on these breakthrough results, how the NTU-65-CoTi might be possible to procure pure C_3H_6 and C_3H_8 are mostly expected. As shown in Fig. 5e, two beds A and B, both packed with NTU-65-CoTi.^{47,48} During the adsorption cycle, the two beds A and B operate sequentially. The operation of Bed A and B should last for at least 130 min g^{-1} and 35 min g^{-1} , respectively. Highly pure C_3H_8 (99.9%, GC limitation) is recovered from Bed B at the end of the adsorption cycle. After termination of the adsorption cycle, both Bed A and B are subjected to counter-current vacuum desorption. From Bed A, the product C_3H_4 with improved concentration (from 0.5% to



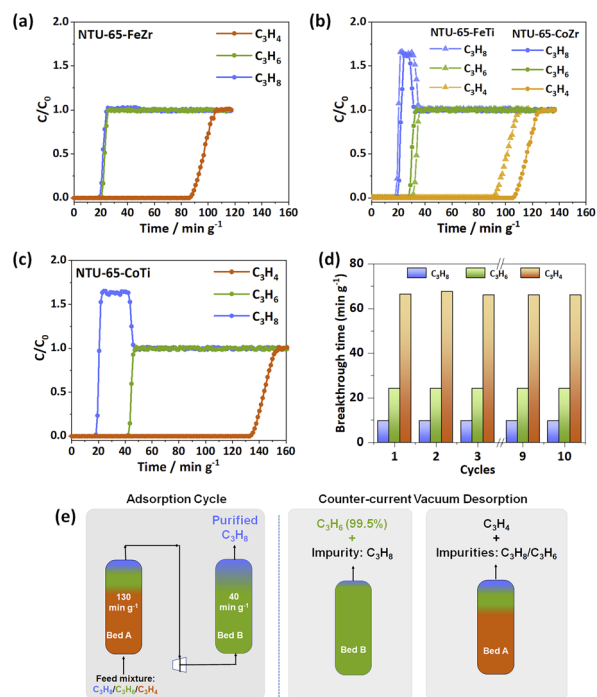


Fig. 5 Breakthrough curves of NTU-65-series (a)–(d) for $C_3H_4/C_3H_6/C_3H_8$ (0.5/49.75/49.75, v/v/v, 2 mL min^{-1}) at 273 K. Cycling performance of NTU-65-CoTi (5 mL min^{-1}) (d). Schematic representation of the separation of C3 ternary mixtures using two packed beds of NTU-65-CoTi in a vacuum swing adsorption process (e).

6.3%) can be obtained, while from Bed B, the product C_3H_6 can be harvested with a purity approaching 99.5%.

Conclusions

In summary, due to the demand for energy-efficient separation of C3 hydrocarbons, we here report a gradient regulation of framework softness *via* the node substitution approach. The exclusive response to C_3H_4 in NTU-65-FeZr has been tailored into a sequential capture of C_3H_4 and C_3H_6 in NTU-65-CoTi. This breakthrough enables an unprecedented ability for sieving separation of the ternary $C_3H_4/C_3H_6/C_3H_8$ mixtures in a single domain. By following designed procedures, highly pure C_3H_8 (99.9%) and C_3H_6 (99.5%) can be obtained. Moving forward, given that the conditions for feasible gas separation vary significantly, the precise understanding and ability to tune the gate-openings of soft PCPs are particularly important, potentially indicating a path to other challenging multi-component systems.

Data availability

The data supporting the findings of this study are available within the article and/or its ESI.†

Author contributions

J. D. conceived the research idea and designed the experiments. S. L. and Y. H. conducted the experiments. S. L., Y. H., J. W.,

Y. L., and J. T. analysed and discussed the data. J. Z. and K. R. performed the calculations. J. D. and K. G. wrote the paper. All authors offered constructive comments on the manuscript.

Conflicts of interest

There are no conflicts to declare.

Acknowledgements

We are thankful for the financial support of the National Natural Science Foundation of China (22171135), the Innovative Research Team Program by the Ministry of Education of China (IRT-17R54), the National Natural Science Foundation of Jiangsu Province (BK20231269), the State Key Laboratory of Materials-Oriented Chemical Engineering (SKL-MCE-23A18) and the Education Department of Henan Province (22A150050 and 2023GGJS131).

Notes and references

- 1 D. S. Sholl and R. P. Lively, *Nature*, 2016, **532**, 435–437.
- 2 Y. Wang, N. Y. Huang, X. W. Zhang, H. He, R. K. Huang, Z. M. Ye, Y. Li, D. D. Zhou, P. Q. Liao, X. M. Chen and J. P. Zhang, *Angew. Chem., Int. Ed.*, 2019, **58**, 7692–7696.
- 3 F. A. Da Silva and A. E. Rodrigues, *AIChE J.*, 2001, **47**, 341–357.
- 4 B. Y. Li, Z. J. Zhang, Y. Li, K. X. Yao, Y. H. Zhu, Z. Y. Deng, F. Yang, X. J. Zhou, G. H. Li, H. H. Wu, N. Nijem, Y. J. Chabal, Z. P. Lai, Y. Han, Z. Shi, S. H. Feng and J. Li, *Angew. Chem., Int. Ed.*, 2012, **51**, 1412–1415.
- 5 G. K. H. Shimizu, J. M. Taylor and S. Kim, *Science*, 2013, **341**, 354–355.
- 6 K. S. Walton, *Nat. Chem.*, 2014, **6**, 277–278.
- 7 S. H. Yang, A. J. Ramirez-Cuesta, R. Newby, V. Garcia-Sakai, P. Manuel, S. K. Callear, S. I. Campbell, C. C. Tang and M. Schroder, *Nat. Chem.*, 2015, **7**, 121–129.
- 8 T. M. McDonald, J. A. Mason, X. Q. Kong, E. D. Bloch, D. Gygi, A. Dani, V. Crocella, F. Giordanino, S. O. Odoh, W. S. Drisdell, B. Vlasisavljevic, A. L. Dzubak, R. Poloni, S. K. Schnell, N. Planas, K. Lee, T. Pascal, L. W. F. Wan, D. Prendergast, J. B. Neaton, B. Smit, J. B. Korrigh, L. Gagliardi, S. Bordiga, J. A. Reimer and J. R. Long, *Nature*, 2015, **519**, 303–308.
- 9 X. L. Cui, K. J. Chen, H. B. Xing, Q. W. Yang, R. Krishna, Z. B. Bao, H. Wu, W. Zhou, X. L. Dong, Y. Han, B. Li, Q. L. Ren, M. J. Zaworotko and B. L. Chen, *Science*, 2016, **353**, 141–144.
- 10 S. Krause, V. Bon, I. Senkovska, U. Stoeck, D. Wallacher, D. M. Tobbens, S. Zander, R. S. Pillai, G. Maurin, F. X. Coudert and S. Kaskel, *Nature*, 2016, **532**, 348–352.
- 11 A. Cadiau, Y. Belmabkhout, K. Adil, P. M. Bhatt, R. S. Pillai, A. Shkurenko, C. Martineau-Corcos, G. Maurin and M. Eddaoudi, *Science*, 2017, **356**, 731–735.
- 12 P.-Q. Liao, N.-Y. Huang, W.-X. Zhang, J.-P. Zhang and X.-M. Chen, *Science*, 2017, **356**, 1193–1196.



- 13 H. Furukawa, K. E. Cordova, M. O'Keeffe and O. M. Yaghi, *Science*, 2013, **341**, 1230444–1230455.
- 14 A. Cadiou, K. Adil, P. M. Bhatt, Y. Belmabkhout and M. Eddaoudi, *Science*, 2016, **353**, 137–140.
- 15 J. E. Bachman, M. T. Kapelewski, D. A. Reed, M. I. Gonzalez and J. R. Long, *J. Am. Chem. Soc.*, 2017, **139**, 15363–15370.
- 16 L. Yang, X. Cui, Q. Yang, S. Qian, H. Wu, Z. Bao, Z. Zhang, Q. Ren, W. Zhou, B. Chen and H. Xing, *Adv. Mater.*, 2018, **30**, 1705374.
- 17 M.-H. Yu, B. Space, D. Franz, W. Zhou, C. He, L. Li, R. Krishna, Z. Chang, W. Li, T.-L. Hu and X.-H. Bu, *J. Am. Chem. Soc.*, 2019, **141**, 17703–17712.
- 18 T. Ke, Q. Wang, J. Shen, J. Zhou, Z. Bao, Q. Yang and Q. Ren, *Angew. Chem., Int. Ed.*, 2020, **59**, 12725–12730.
- 19 H. Zeng, M. Xie, T. Wang, R.-J. Wei, X.-J. Xie, Y. Zhao, W. Lu and D. Li, *Nature*, 2021, **595**, 542–548.
- 20 Q. Dong, Y. Huang, J. Wan, Z. Lu, Z. Wang, C. Gu, J. Duan and J. Bai, *J. Am. Chem. Soc.*, 2023, **145**, 8043–8051.
- 21 H. Wang, X. L. Dong, V. Colombo, Q. N. Wang, Y. Y. Liu, W. Liu, X. L. Wang, X. Y. Huang, D. M. Proserpio, A. Sironi, Y. Han and J. Li, *Adv. Mater.*, 2018, **30**, 1805088–1805096.
- 22 D. Antypov, A. Shkurenko, P. M. Bhatt, Y. Belmabkhout, K. Adil, A. Cadiou, M. Suyetin, M. Eddaoudi, M. J. Rosseinsky and M. S. Dyer, *Nat. Commun.*, 2020, **11**, 6099.
- 23 X. Li, J. Liu, K. Zhou, S. Ullah, H. Wang, J. Zou, T. Thonhauser and J. Li, *J. Am. Chem. Soc.*, 2022, **144**, 21702–21709.
- 24 K. J. Chen, D. G. Madden, S. Mukherjee, T. Pham, K. A. Forrest, A. Kumar, B. Space, J. Kong, Q. Y. Zhang and M. J. Zaworotko, *Science*, 2019, **366**, 241–246.
- 25 R. Kitaura, K. Seki, G. Akiyama and S. Kitagawa, *Angew. Chem., Int. Ed.*, 2003, **42**, 428–431.
- 26 S. Kitagawa and M. Kondo, *Bull. Chem. Soc. Jpn.*, 1998, **71**, 1739–1753.
- 27 S. Horike, S. Shimomura and S. Kitagawa, *Nat. Chem.*, 2009, **1**, 695–704.
- 28 N. Behera, J. Duan, W. Jin and S. Kitagawa, *EnergyChem*, 2021, **3**, 100067.
- 29 V. I. Nikolayenko, D. C. Castell, D. Sensharma, M. Shivanna, L. Loots, K. A. Forrest, C. J. Solanilla-Salinas, K. I. Otake, S. Kitagawa, L. J. Barbour, B. Space and M. J. Zaworotko, *Nat. Chem.*, 2023, **15**, 542–549.
- 30 D. D. Zhou, P. Chen, C. Wang, S. S. Wang, Y. Du, H. Yan, Z. M. Ye, C. T. He, R. K. Huang, Z. W. Mo, N. Y. Huang and J. P. Zhang, *Nat. Mater.*, 2019, **18**, 994–998.
- 31 L. B. Li, R. B. Lin, R. Krishna, X. Q. Wang, B. Li, H. Wu, J. P. Li, W. Zhou and B. L. Chen, *J. Am. Chem. Soc.*, 2017, **139**, 7733–7736.
- 32 J. A. Mason, J. Oktawiec, M. K. Taylor, M. R. Hudson, J. Rodriguez, J. E. Bachman, M. I. Gonzalez, A. Cervellino, A. Guagliardi, C. M. Brown, P. L. Llewellyn, N. Masciocchi and J. R. Long, *Nature*, 2015, **527**, 357–361.
- 33 J. H. Lee, S. Jeoung, Y. G. Chung and H. R. Moon, *Coord. Chem. Rev.*, 2019, **389**, 161–188.
- 34 M. Bonneau, C. Lavenn, J.-J. Zheng, A. Legrand, T. Ogawa, K. Sugimoto, F.-X. Coudert, R. Reau, S. Sakaki, K.-i. Otake and S. Kitagawa, *Nat. Chem.*, 2022, **14**, 816–822.
- 35 A. Schneemann, V. Bon, I. Schwedler, I. Senkovska, S. Kaskel and R. A. Fischer, *Chem. Soc. Rev.*, 2014, **43**, 6062–6096.
- 36 Y. Huang, J. Wan, T. Pan, K. Ge, Y. Guo, J. Duan, J. Bai, W. Jin and S. Kitagawa, *J. Am. Chem. Soc.*, 2023, **145**, 24425–24432.
- 37 J. Wan, H. L. Zhou, K. Hyeon-Deuk, I. Y. Chang, Y. Huang, R. Krishna and J. Duan, *Angew. Chem., Int. Ed.*, 2023, **62**, e202316792.
- 38 M. J. Kalmutzki, N. Hanikel and O. M. Yaghi, *Sci. Adv.*, 2018, **4**, eaat9180.
- 39 A. L. Spek, *J. Appl. Crystallogr.*, 2003, **36**, 7–13.
- 40 S. Sen, N. Hosono, J. J. Zheng, S. Kusaka, R. Matsuda, S. Sakaki and S. Kitagawa, *J. Am. Chem. Soc.*, 2017, **139**, 18313–18321.
- 41 C. Gu, N. Hosono, J. J. Zheng, Y. Sato, S. Kusaka, S. Sakaki and S. Kitagawa, *Science*, 2019, **363**, 387–391.
- 42 Q. Dong, X. Zhang, S. Liu, R. B. Lin, Y. Guo, Y. Ma, A. Yonezu, R. Krishna, G. Liu, J. Duan, R. Matsuda, W. Jin and B. Chen, *Angew. Chem. Int. Ed. Engl.*, 2020, **59**, 22756–22762.
- 43 C. Kang, Z. Zhang, S. Kusaka, K. Negita, A. K. Usadi, D. C. Calabro, L. S. Baugh, Y. Wang, X. Zou, Z. Huang, R. Matsuda and D. Zhao, *Nat. Mater.*, 2023, **22**, 636–643.
- 44 J. J. Zheng, S. Kusaka, R. Matsuda, S. Kitagawa and S. Sakaki, *J. Am. Chem. Soc.*, 2018, **140**, 13958–13969.
- 45 T. Ke, Q. J. Wang, J. Shen, J. Y. Zhou, Z. B. Bao, Q. W. Yang and Q. L. Ren, *Angew. Chem., Int. Ed.*, 2020, **59**, 12725–12730.
- 46 F. Zheng, R. Chen, Y. Liu, Q. Yang, Z. Zhang, Y. Yang, Q. Ren and Z. Bao, *Adv. Sci.*, 2023, **10**, 2207127.
- 47 E. D. Bloch, W. L. Queen, R. Krishna, J. M. Zadrozny, C. M. Brown and J. R. Long, *Science*, 2012, **335**, 1606–1610.
- 48 R. Krishna, *ACS Omega*, 2020, **5**, 16987–17004.



Supplementary Information

Fine-regulating of gradient gate-opening in nanoporous crystals for sieving separation of ternary C3 hydrocarbons

Shuang Liu,^{a,+} Yuhang Huang,^{b,+} Jingmeng Wan,^b Jia-jia Zheng,^c Rajamani Krishna,^d Yi Li,^b Kai Ge,^{b,*} Jie Tang,^b
Jingui Duan^{b,*}

^a Henan Engineering Research Centre for Green Synthesis of Pharmaceuticals, College of Chemistry and Chemical Engineering, Shangqiu Normal University, Shangqiu, 476000, China.

^b State Key Laboratory of Materials-Oriented Chemical Engineering, College of Chemical Engineering, Nanjing Tech University, Nanjing, 211816, China.

^c Laboratory of Theoretical and Computational Nanoscience, CAS Center for Excellence in Nanoscience, National Center for Nanoscience and Technology, Chinese Academy of Sciences, Beijing 100190, China.

^d Van 't Hoff Institute for Molecular Sciences, University of Amsterdam, Science Park 904, 1098 XH Amsterdam, The Netherlands.

Email: gekai@njtech.edu.cn (K. G.); duanjingui@njtech.edu.cn (J. D.)

General Procedures and Materials

All reagents and solvents were commercially available and used as received. The Fourier-transform Infrared (FT-IR) spectra were recorded from KBr pellets in the range of 4000–600 cm^{-1} on a VECTOR 22 spectrometer. Thermogravimetric analyses (TGA) were performed using a STA 209 F1 (NETZSCH Instruments) thermo-microbalance, heating from room temperature to 650°C at a rate of 10°C min^{-1} under nitrogen flow. Simulated powder patterns from single-crystal X-ray diffraction data were generated using Mercury 1.4.2 software. The coincident PXRD/adsorption measurements were performed with a Rigaku SmartLab with $\text{CuK}\alpha$ radiation connected to a BELSORP-18PLUS volumetric adsorption setup (MicrotracBEL Japan, Inc.) equipped with a custom-made cryostat apparatus. The respective apparatuses were synchronized to enable each PXRD pattern to be obtained at each equilibrium point of the sorption isotherms.

Synthesis of NTU-65-series. A solution of **L** (0.50 mmol) in *N, N'*-dimethylformamide (DMF) (1 mL) was slowly layered on aqueous solution (0.5 mL) of $\text{M1}(\text{BF}_6)_2 \cdot 6\text{H}_2\text{O}$ (0.014 mmol, M1: Fe^{2+} , Co^{2+}) and $(\text{NH}_4)_2\text{M2F}_6 \cdot 6\text{H}_2\text{O}$ (0.014 mmol, M2: Zr^{4+} , Ti^{4+}). After a week, single-crystals of NTU-65 derivatives (named as **NTU-65-FeZr**, **NTU-65-FeTi**, **NTU-65-CoZr** and **NTU-65-CoTi**, respectively) were obtained. Yield: ~40-60%, based on **L**.

Single crystal X-ray studies. Single-crystal X-ray diffraction measurements were performed on a Bruker Smart Apex CCD diffractometer at 298 K using graphite monochromator $\text{Mo}/\text{K}\alpha$ radiation ($\lambda = 0.71073 \text{ \AA}$). Data reduction was made with the Bruker SAINT program. The structures were solved by direct methods and refined with full-matrix least squares technique using the SHELXTL package¹. Non-hydrogen atoms were refined with anisotropic displacement parameters during the final cycles. Organic hydrogen atoms were placed in calculated positions with isotropic displacement parameters set to $1.2 \times U_{\text{eq}}$ of the attached atom. The unit cell includes disordered solvent molecules, which could not be modeled as discrete atomic sites. We employed PLATON/SQUEEZE^{2, 3} to calculate the diffraction contribution of the solvent molecules and, thereby, to produce a set of solvent-free diffraction intensities; structures were then refined again using the data generated. Crystal data are summarized in Table S1.

Activation of NTU-65-series. Solvent-exchanged crystal was prepared by immersing the as-synthesized samples in dry MeOH for two days to remove the nonvolatile solvents, and the extract

was decanted every 8 h and fresh acetone was replaced. The completely activated sample was obtained by heating the solvent-exchanged sample at 25°C for 6 h, 60°C for 6 h and then 120°C for 20 h under a dynamic high vacuum.

Single-gas sorption measurements. Gas adsorptions were performed on a Belsorp volumetric adsorption instrument (BEL Japan Corp.). In the sorption measurements, ultra-high-purity grade gases were used throughout the experiments.

In-situ X-ray study. The fully activated crystals that loaded inside a double-layer sealed beryllium ball were purged by C₃H₄ at 273 K, respectively. The X-ray diffractions were then collected at different pressures according to the corresponding isotherms. The system pressure was regulated by a controller that contains an automatic dosing system and pressure sensor (0.01-100 kPa). For each measurement, PXRD was collected at 20 min later, after adsorption reaches equilibrium at this pressure.

Fitting of unary isotherm data. The unary isotherm data for C₃H₄, C₃H₆ and C₃H₈, measured at three different temperatures 273 K, 283 K, and 298 K in **NTU-65-FeZr**, **NTU-65-FeTi**, **NTU-65-CoZr** and **NTU-65-CoTi** were fitted with good accuracy using the dual-site Langmuir-Freundlich model, where we distinguish two distinct adsorption sites A and B:

$$q = \frac{q_{sat,A} b_A p^{v_A}}{1 + b_A p^{v_A}} + \frac{q_{sat,B} b_B p^{v_B}}{1 + b_B p^{v_B}} \quad (S1)$$

In eq (S1), the Langmuir-Freundlich parameters b_A, b_B are both temperature dependent

$$b_A = b_{A0} \exp\left(\frac{E_A}{RT}\right); \quad b_B = b_{B0} \exp\left(\frac{E_B}{RT}\right) \quad (S2)$$

In eq (S2), E_A, E_B are the energy parameters associated with sites A, and B, respectively.

The fit parameters are provided in Table S4-S7,

Isosteric heat of adsorption. The isosteric heat of adsorption, Q_{st} , is defined as

$$Q_{st} = -RT^2 \left(\frac{\partial \ln p}{\partial T} \right)_q \quad (S3)$$

where the derivative in the right member of eq (S3) is determined at constant adsorbate loading, q . The derivative was determined by analytic differentiation of the combination of eq (S1), eq (S2), and eq (S3).

IAST selectivities. The IAST was used to determine the selectivities for binary 50/50 C₃H₆/C₃H₈ and 1/99 C₃H₄/C₃H₆ mixtures at 273 K, 283 K, and 298 K.

Transient breakthrough simulations. Transient breakthrough experiments were carried out for binary 50/50 C₃H₆/C₃H₈ and 1/99 C₃H₄/C₃H₆ mixtures at a total pressure of 100 kPa and 273 K. The sample mass of MOF in the packed bed, m_{ads} is 1 g. The flow rates at the inlet, $Q_0 = 5 \text{ mL min}^{-1}$. Transient breakthrough simulations were carried out using the methodology described in earlier publications.⁴⁻⁸ In these simulations, intra-crystalline diffusion influences are ignored.

Breakthrough measurements. All experiments were performed on a breakthrough instrument (CT-4, Xuzhou North Gaorui). The initial activated series crystals were tightly packed into a stainless-steel column ($\phi = 0.5 \text{ cm}$, $L = 16.0 \text{ cm}$). Then, the column was activated under vacuum at corresponding temperature and then swept with He flow to remove impurities. Until no any signal was detected, the gas flow was dosed into the column. Breakpoints were determined by gas chromatography. Between cycling experiments, regeneration can be achieved under vacuum at 393 K for 2 h.

Computational Details. Adsorption energies for C₃H₄ were calculated to understand the order in softness of **NTU-65-series**. We carried out canonical Monte-Carlo (MC) simulation⁹ to locate C₃H₄ positions in these PCPs, as implemented in RASPA.¹⁰ The Lennard-Jones (LJ) potentials were used to describe the Van der Waals interaction of gas molecules with PCP framework and the electrostatic interaction was evaluated with the Ewald summation method. The LJ parameters for PCP framework were taken from the standard universal force field (UFF)¹¹ and the DDEC atomic charges¹² of PCP framework were used in the evaluation of electrostatic interaction. The LJ parameters and atomic charges of C₃H₄ were taken from literature.¹³ In the MC simulation, the first 1×10^5 cycles were employed for obtaining equilibration and then 3×10^5 cycles were used for obtaining distribution of guest molecule. The final gas adsorption configuration obtained by above MC simulation was used

to construct the initial structure for performing geometry optimization with density functional theory (DFT).

The Perdew-Burke-Ernzerhof functional¹⁴ with Grimme's semi-empirical "D3" dispersion term¹⁵ (PBE-D3), as implemented in the Vienna Ab initio Simulation Package (VASP 5.4.1),^{16,17} was employed in these calculations. The plane wave basis sets with an energy cutoff of 500 eV were used to describe valence electrons and the projector-augmented-wave pseudopotentials^{18,19} were used to describe core electrons. The criterion of atomic force for geometry optimization was set to be 0.02 eV/Å. The Brillouin zone was sampled by a Γ -point in these calculations. Hubbard U corrections²⁰ were applied to the d electrons of Ti, Fe, Co, and Zr atoms with U_{eff} values of 3.0, 4.0, 3.3, and 3.0 eV, respectively.²¹
²² Upon optimized structures, the binding energies (BE) were calculated with eq. S4;

$$BE = E(\text{PCP} \cdot n\text{C}_3\text{H}_4)_{\text{eq}} / n - E(\text{PCP})_{\text{eq}} / n - E(\text{G})_{\text{eq}} \quad (\text{S4})$$

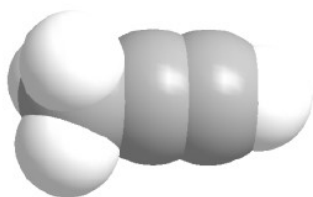
where $E(\text{PCP} \cdot n\text{C}_3\text{H}_4)_{\text{eq}}$ is the total energy of PCPs with n gas molecules per unit cell, $E(\text{PCP})_{\text{eq}}$ and $E(\text{G})_{\text{eq}}$ are the total energies of empty PCPs in the closed phase and one free gas molecule, respectively, and the subscript "eq" represents the equilibrium structure. Because the closed phases of these PCPs are difficult to obtain in experiment, we started from the reported analogy of these PCPs and replaced the corresponding atoms with Fe/Co and Ti/Zr, respectively. The structures of open phases of PCPs were taken from our experimental results.

Table S1. Crystal information of NTU-65-series

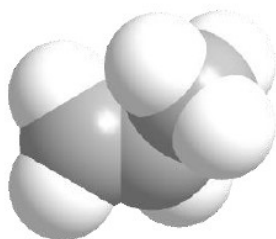
	NTU-65-FeZr	NTU-65-FeTi	NTU-65-CoZr	NTU-65-CoTi
Empirical formula	C ₂₄ H ₂₀ Fe F ₆ N ₈ Zr	C ₂₄ H ₂₀ Fe F ₆ N ₈ Ti	C ₂₄ H ₂₀ Co F ₆ N ₈ Zr	C ₂₄ H ₂₀ Co F ₆ N ₈ Ti
Formula weight	681.55	638.20	684.63	641.31
Crystal system	monoclinic	monoclinic	monoclinic	monoclinic
Space group	<i>P2₁/c</i>	<i>C 2/m</i>	<i>P2₁/c</i>	<i>P2₁/c</i>
	<i>a</i> =13.709(8)	<i>a</i> =12.599(6)	<i>a</i> =13.517(16)	<i>a</i> =13.667(8)
Unit cell dimensions (Å)	<i>b</i> =25.837(15)	<i>b</i> =25.838(11)	<i>b</i> =25.270(3)	<i>b</i> =25.634(14)
	<i>c</i> =12.830(8)	<i>c</i> =13.639(6)	<i>c</i> =12.693(15)	<i>c</i> =12.720(7)
	<i>β</i> =117.798(7)	<i>β</i> =116.756(5)	<i>β</i> =117.986(16)	<i>β</i> =115.987(8)
Volume (Å ³)	4020(4)	3965(3)	3829(8)	4006(4)
Z	4	4	4	4
Density (calculated) (g/cm ³)	1.126	1.069	1.188	1.063
Mu (MoKa) (mm ⁻¹)	0.711	0.711	0.711	0.711
<i>F</i> ₍₀₀₀₎	1360	1288	1364	1292
Theta min-max	2.926, 27.812	2.979, 28.367	1.611, 24.549	1.589, 25.099
	-15<= <i>h</i> <=11	-9<= <i>h</i> <=16	-15<= <i>h</i> <=14	-16<= <i>h</i> <=15
Index ranges	-29<= <i>k</i> <=25	-32<= <i>k</i> <=34	-29<= <i>k</i> <=29	-30<= <i>k</i> <=28
	-14<= <i>l</i> <=14	-18<= <i>l</i> <=18	-14<= <i>l</i> <=10	-15<= <i>l</i> <=15
Tot , Uniq Data, <i>R</i> (int)	16998, 5968, 0.131	11793, 4959, 0.085	17589, 6235, 0.113	29051, 7125, 0.095
Observed data [<i>I</i> > 2σ (<i>I</i>)]	3282	2630	3123	3638
<i>N</i> _{ref} , <i>N</i> _{par}	5968, 362	4959, 183	6235, 361	7125, 361
<i>R</i> ₁ , <i>wR</i> ₂ , <i>S</i>	0.1491, 0.3762,	0.0835, 0.2385,	0.0775, 0.1684, 1.02	0.0591, 0.1635,
	1.08	1.04		1.01
Max Shift	0	0	0	0

$$R = \sum ||F_o| - |F_c|| / \sum |F_o|, wR = \{\sum [w (|F_o|^2 - |F_c|^2)^2] / \sum [w (|F_o|^4)]\}^{1/2} \text{ and } w = 1 / [\sigma^2(F_o^2) + (0.1452P)^2]$$

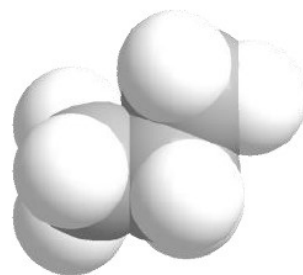
$$\text{where } P = (F_o^2 + 2F_c^2) / 3$$



4.16×4.01×6.51 Å³



3.80×4.00×6.50 Å³



4.00×4.52×6.61 Å³

Figure S1. Comparison of the molecular size and shape of C₃H₄, C₃H₆ and C₃H₈.

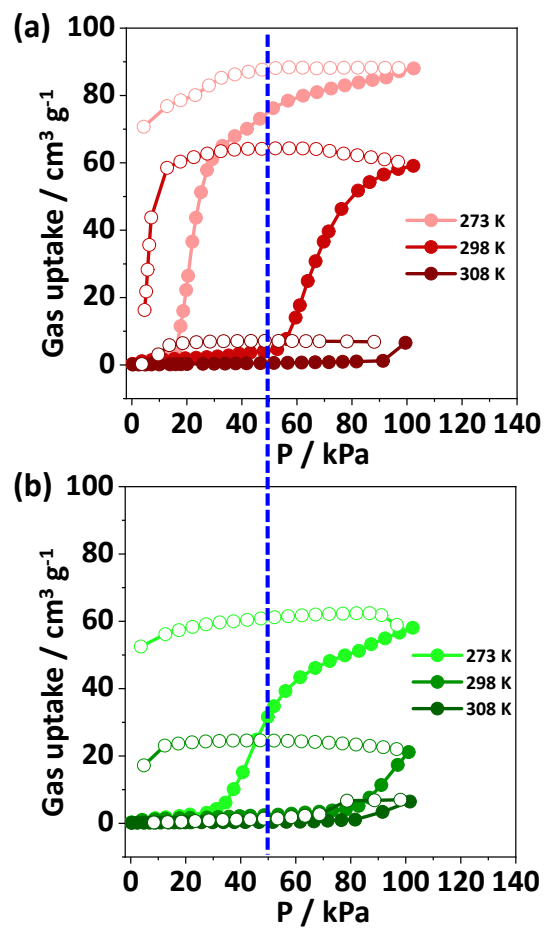


Figure S2. Single-component C₃H₆ (a) and C₃H₈ (b) isotherms of NTU-65 at different temperatures.

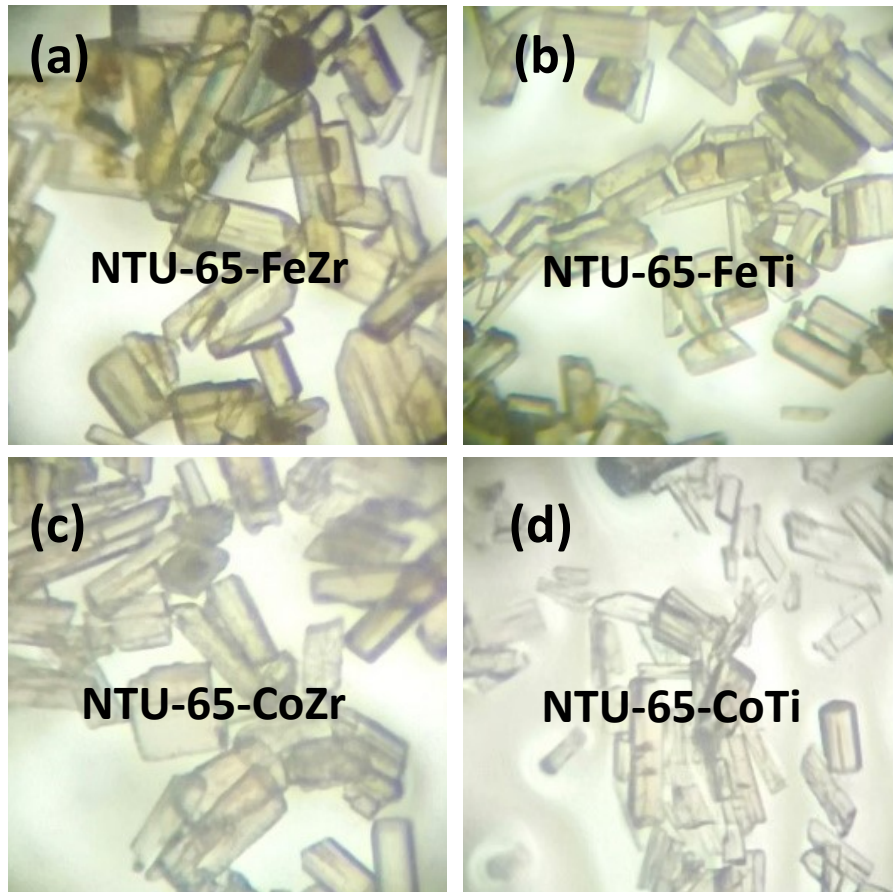


Figure S3. Photos of NTU-65-series.

Structure view of NTU-65-series

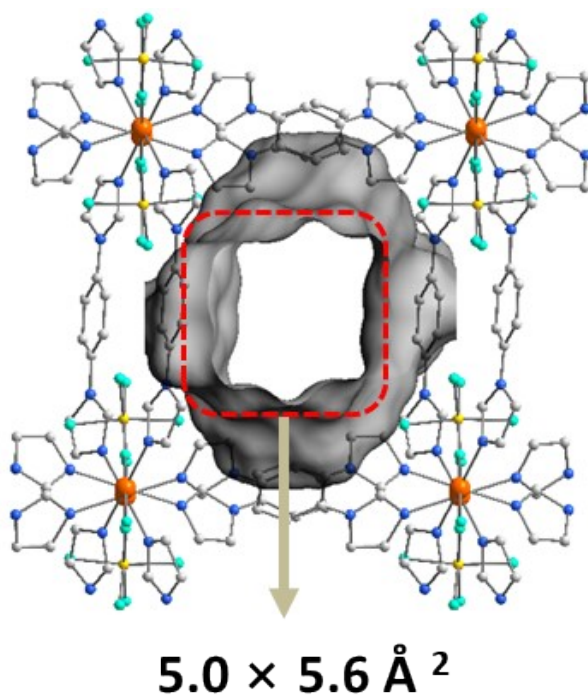
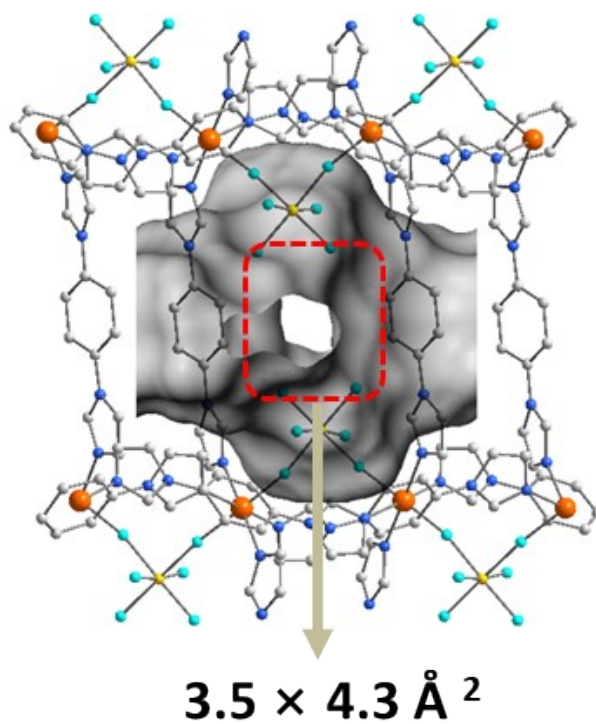


Figure S4. Two kinds of channels in **NTU-65-FeZr**, where the accessible nanospace was highlighted by gray.

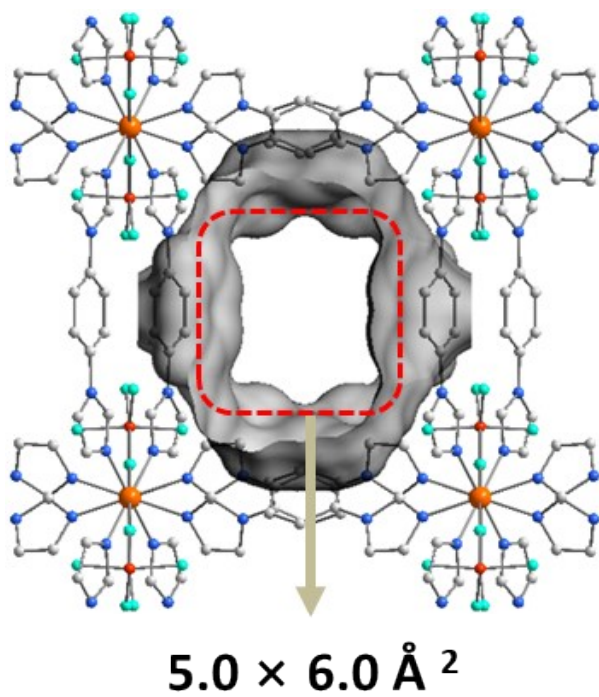
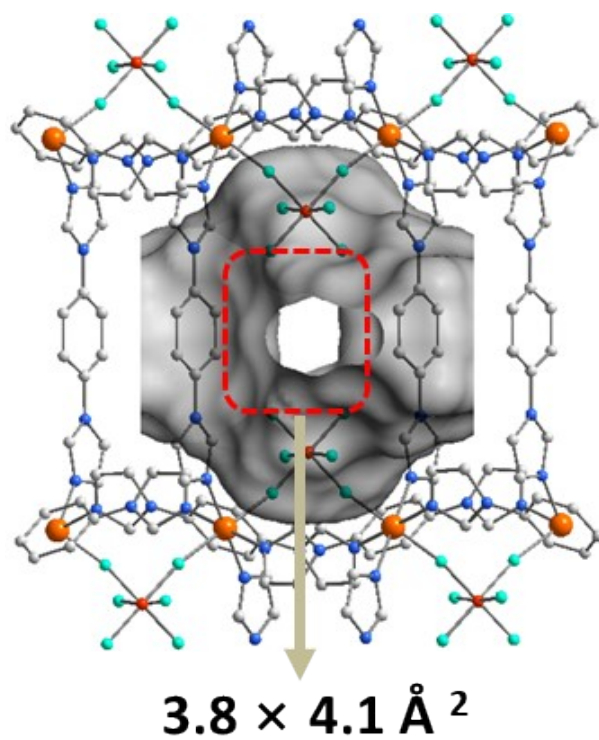


Figure S5. Two kinds of channels in NTU-65-FeTi, where the accessible nanospace was highlighted by gray.

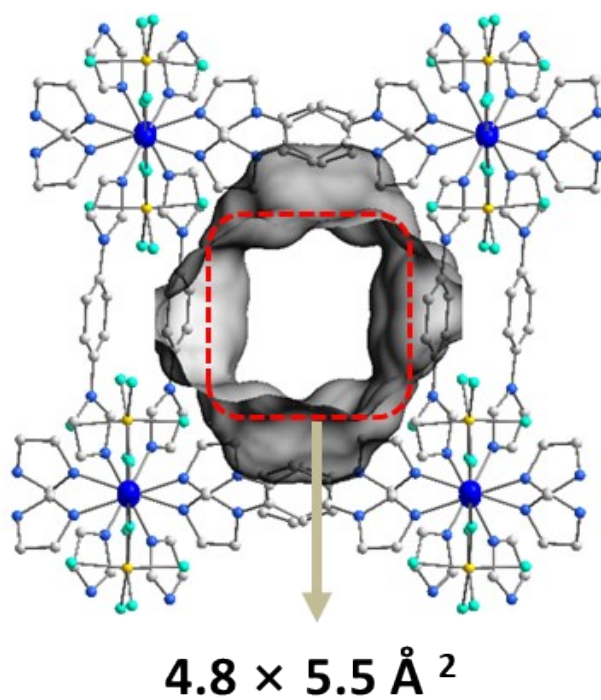
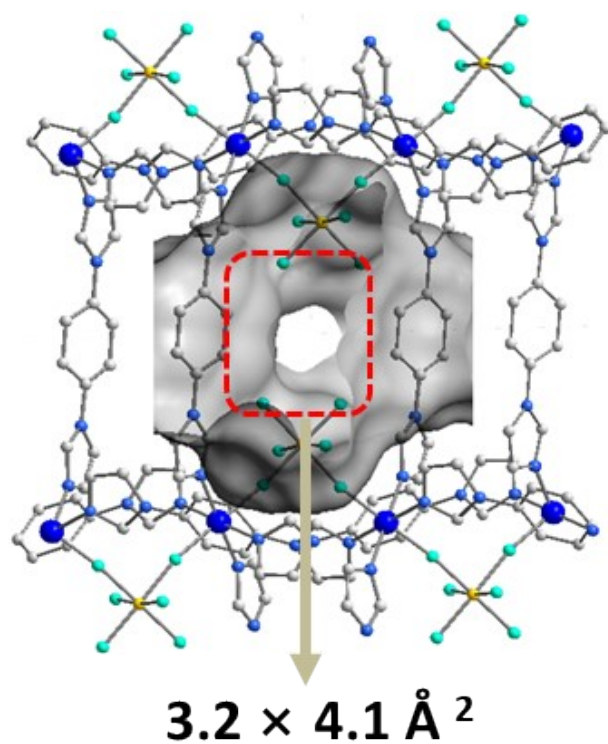


Figure S6. Two kinds of channels in **NTU-65-CoZr**, where the accessible nanospace was highlighted by gray.

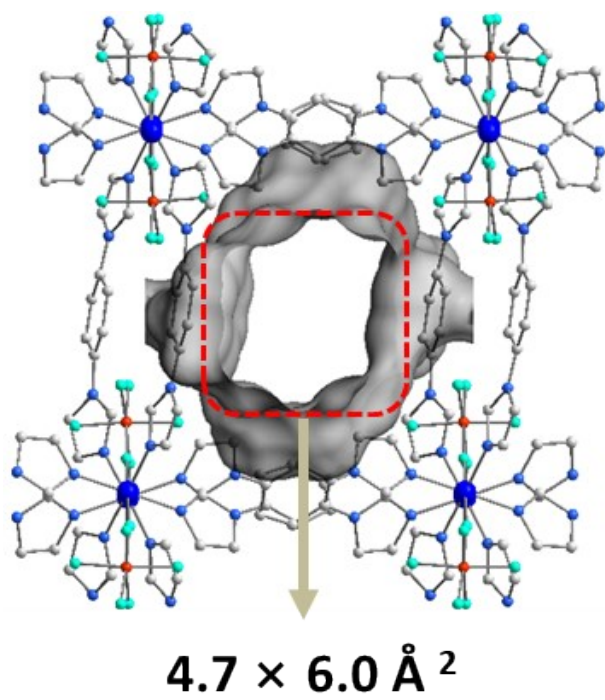
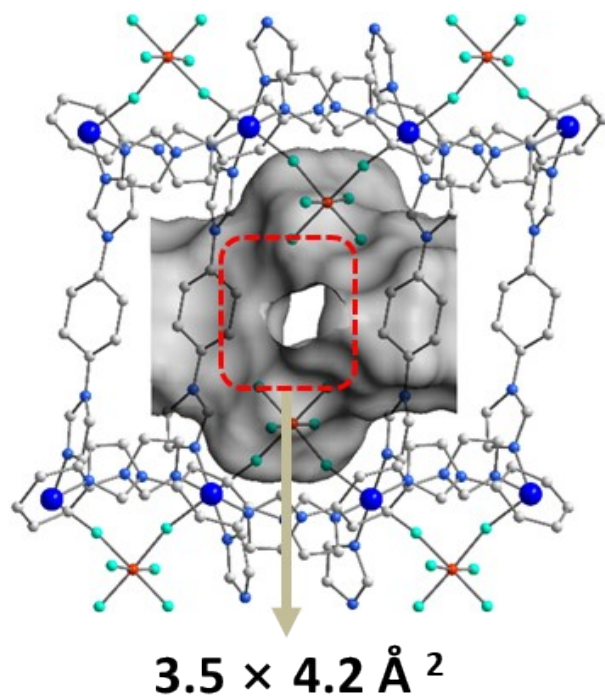


Figure S7. Two kinds of channels in **NTU-65-CoTi**, where the accessible nanospace was highlighted by gray.

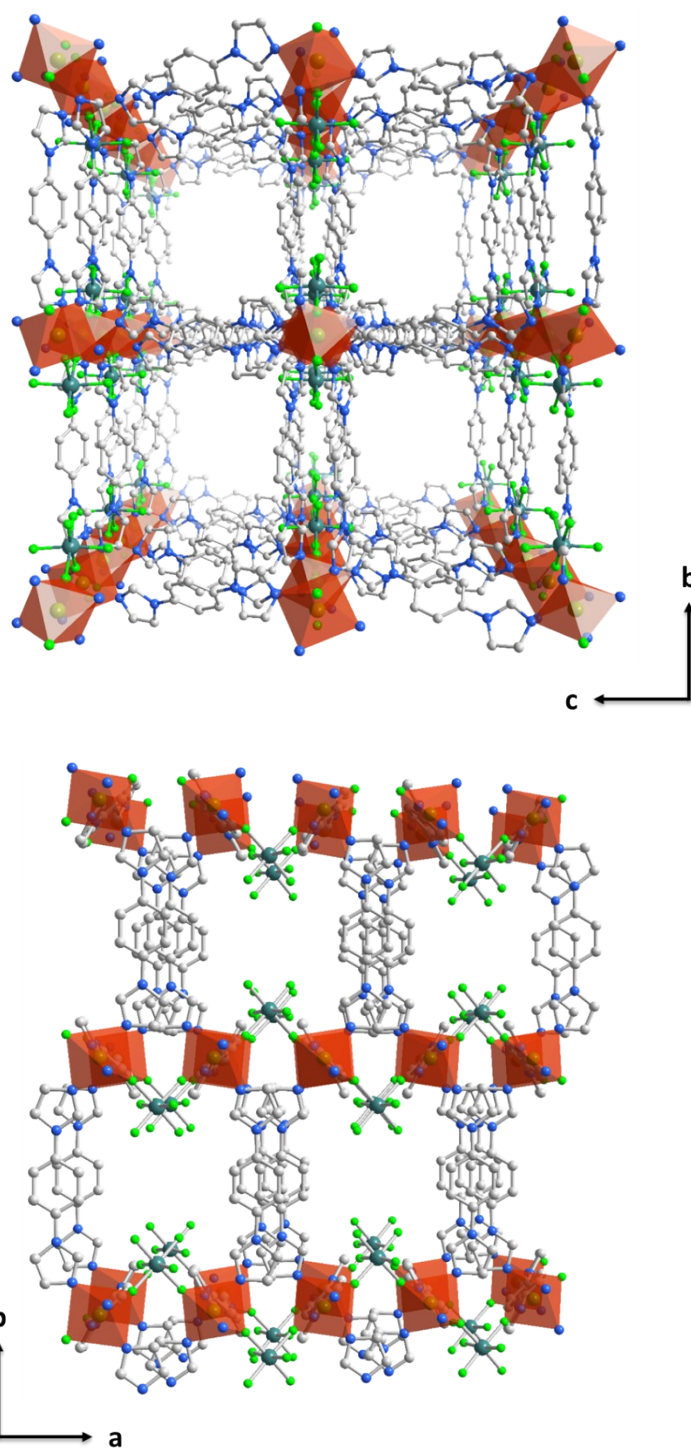


Figure S8. Packing view of the as-synthesized **NTU-65-series** framework along different directions.

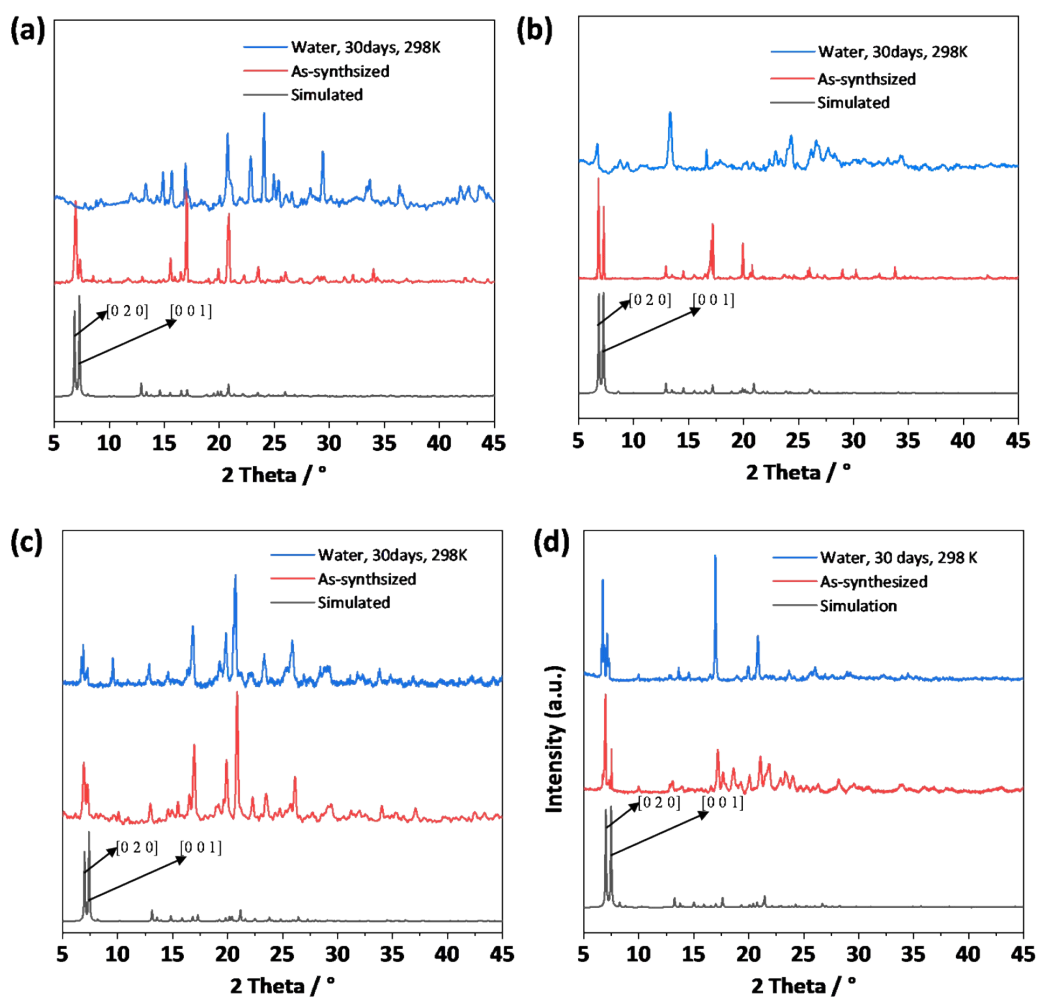


Figure S9. PXRD patterns of **NTU-65-FeZr** (a), **NTU-65-FeTi** (b), **NTU-65-CoZr** (c) and **NTU-65-CoTi** (d): simulated, as-synthesized and soak in water for 30 days at 298 K samples. Phase purity of the bulk crystals was identified by a comparison of the experimental and simulated patterns. The activated phases are still high crystalline materials, and only the position of some diffraction peaks has shifted, indicating structural change after solvent removal.

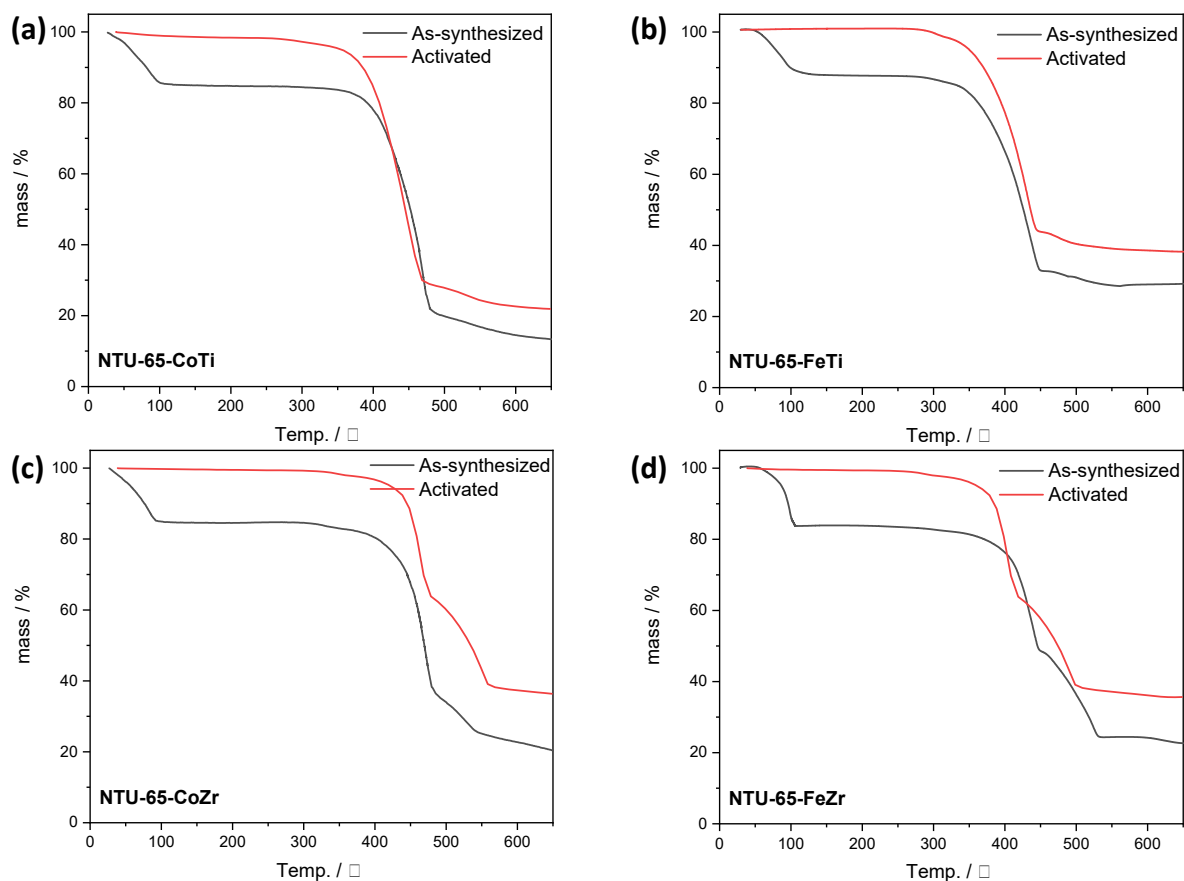


Figure S10. TG curves of **NTU-65-FeZr** (a), **NTU-65-FeTi** (b), **NTU-65-CoZr** (c) and **NTU-65-CoTi** (d).

According to these results, activated phases of the four MOFs can be obtained by degassing methanol exchanged crystals under high vacuum at 120 °C for 20 h.

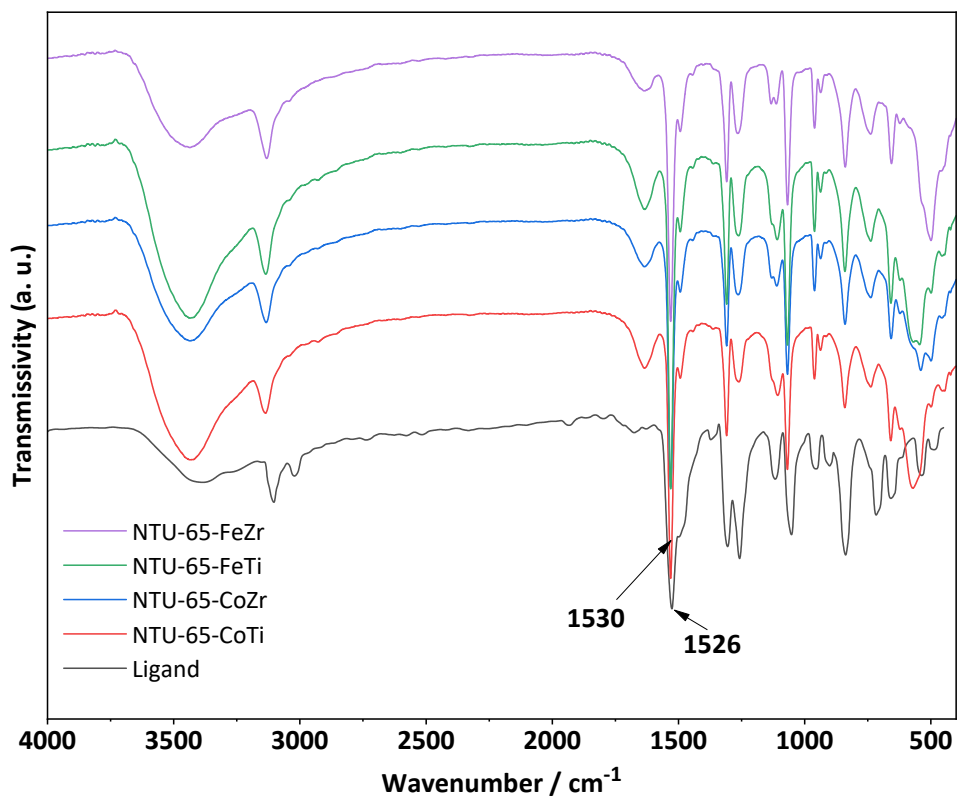


Figure S11. Infrared spectra of ligand and **NTU-65-series**.

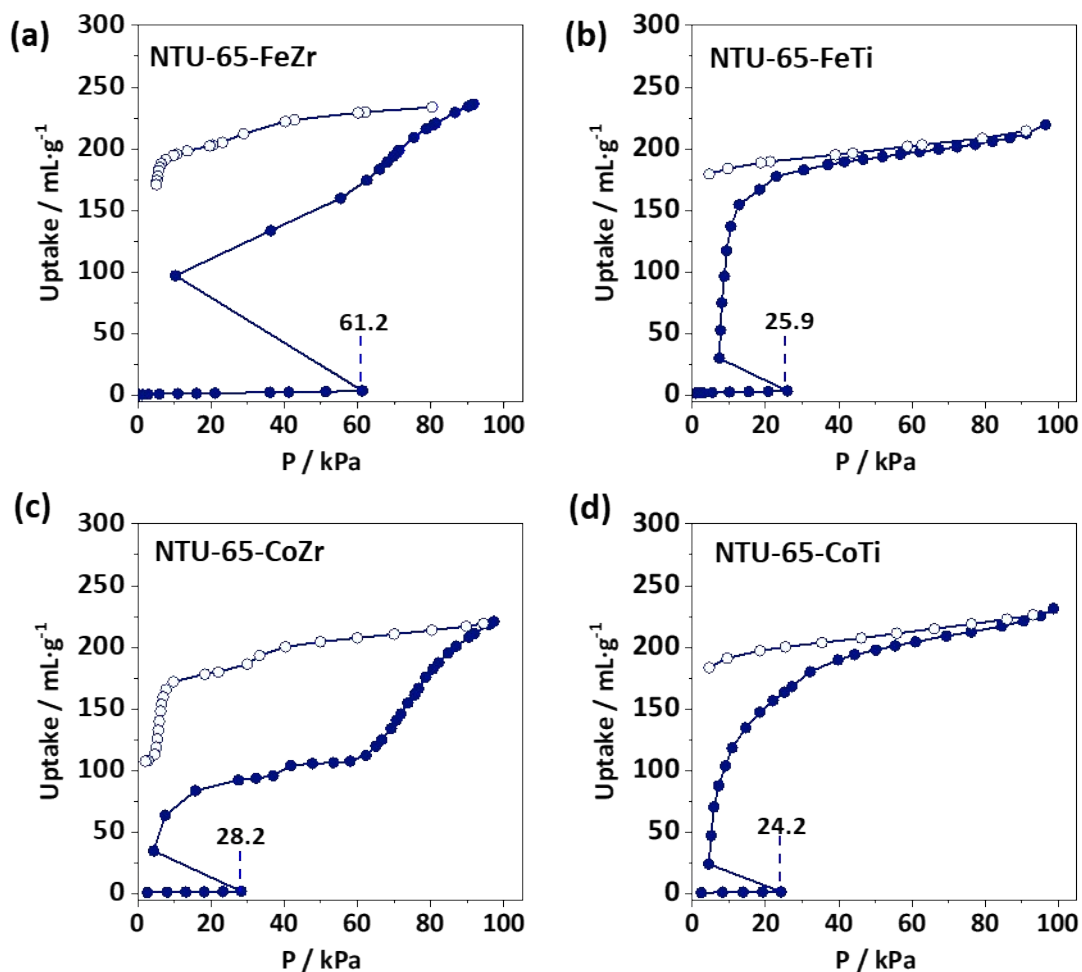


Figure S12. N₂ adsorption isotherms of **NTU-65-series** at 77 K. A 'kink' phenomenon occurred on all of them. Compared to the polar N₂ probe (77 K), CO₂ molecule with large quadrupole-moment ($-13.4 \times 10^{-40} \text{ C m}^2$) may interact with the electronegative F sites of the frameworks in a relatively strong manner. Therefore, the instantaneous gate-opening triggered by N₂ at 77 K may change to a gradual opening following an increase pressure of CO₂, yielding eliminated "kink" phenomenon (Figure 2 in draft).

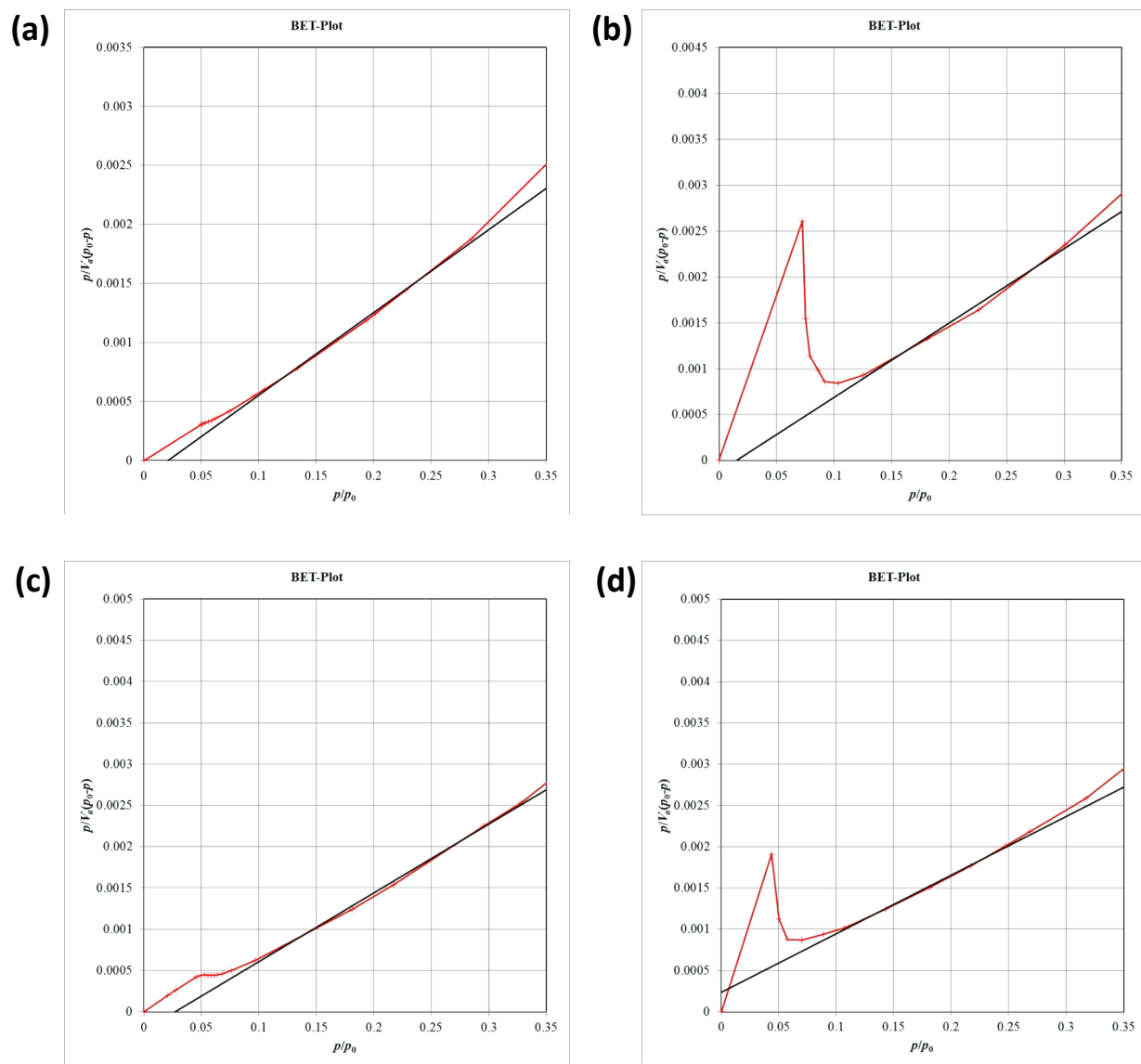


Figure S13. The consistency plots for BET fitting for **NTU-65-FeZr** (a), **NTU-65-FeTi** (b), **NTU-65-CoZr** (c) and **NTU-65-CoTi** (d).

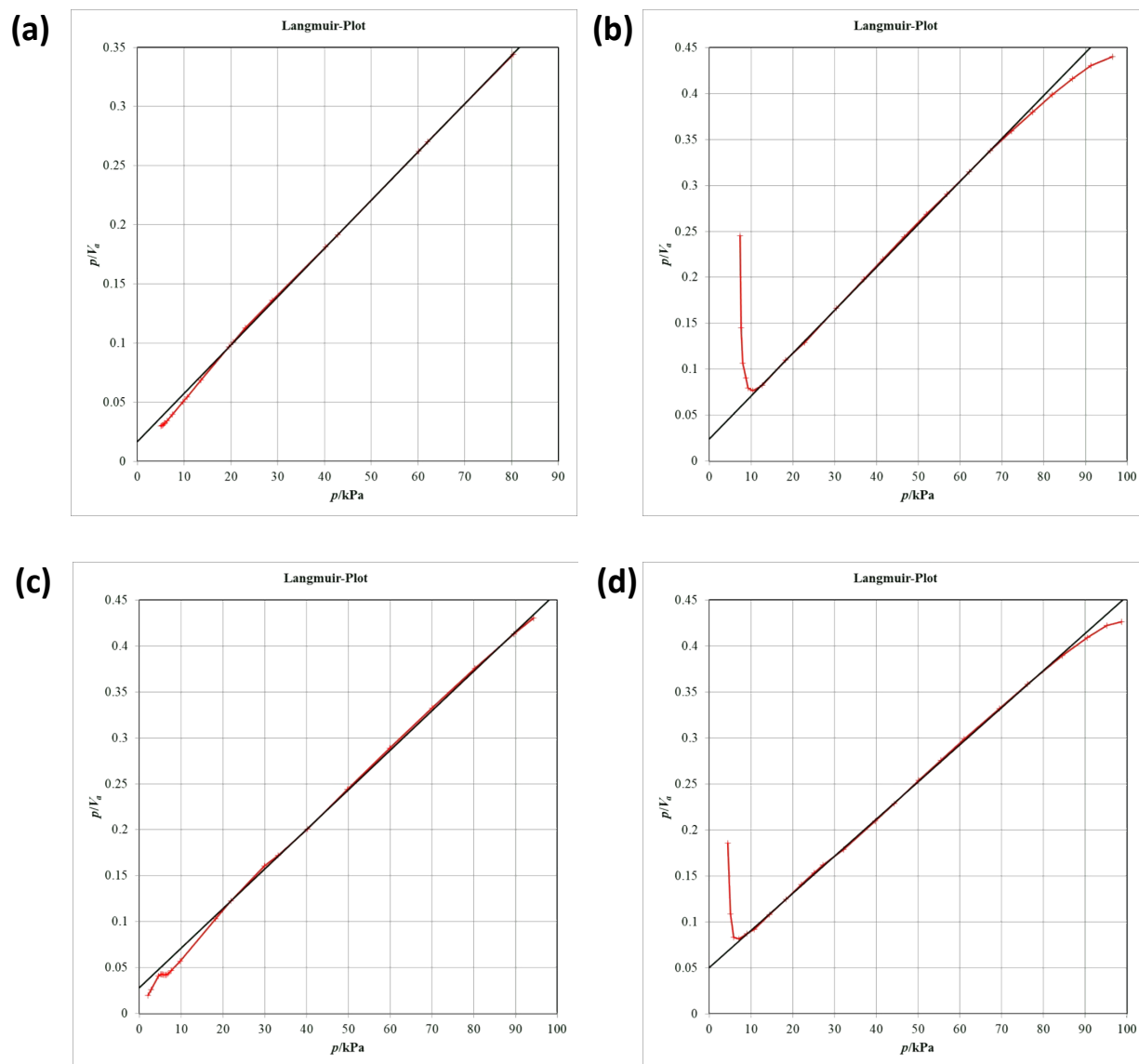


Figure S14. The consistency plots for Langmuir fitting for **NTU-65-FeZr** (a), **NTU-65-FeTi** (b), **NTU-65-CoZr** (c) and **NTU-65-CoTi** (d).

Table S2. The specific surface area and pore volume of **NTU-65-series**.

Materials	$S_{\text{BET}} (\text{m}^2 \cdot \text{g}^{-1})$	$S_{\text{Langmuir}} (\text{m}^2 \cdot \text{g}^{-1})$	$V_t (\text{cm}^3 \cdot \text{g}^{-1})$
NTU-65-FeZr	635.0	1066.1	0.3615
NTU-65-FeTi	545.3	931.8	0.3395
NTU-65-CoZr	537.3	1011.9	0.3392
NTU-65-CoTi	592.7	1078.5	0.3579

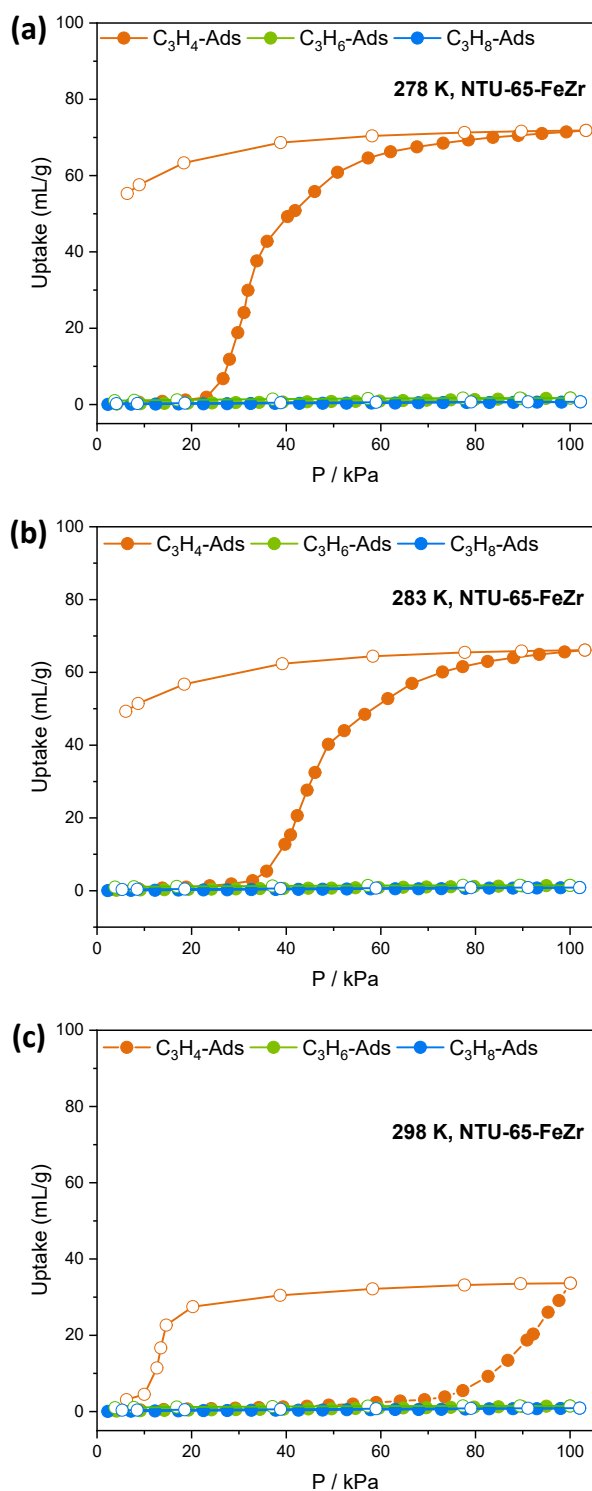


Figure S15. Single-component C_3H_4 , C_3H_6 and C_3H_8 isotherms of **NTU-65-FeZr** at 278 (a), 283 (b), and 298 K (c). Following increased temperature, the gate-opening of C_3H_4 becomes late, however, both C_3H_6 and C_3H_8 can not open the framework threshold the pressure under these temperatures.

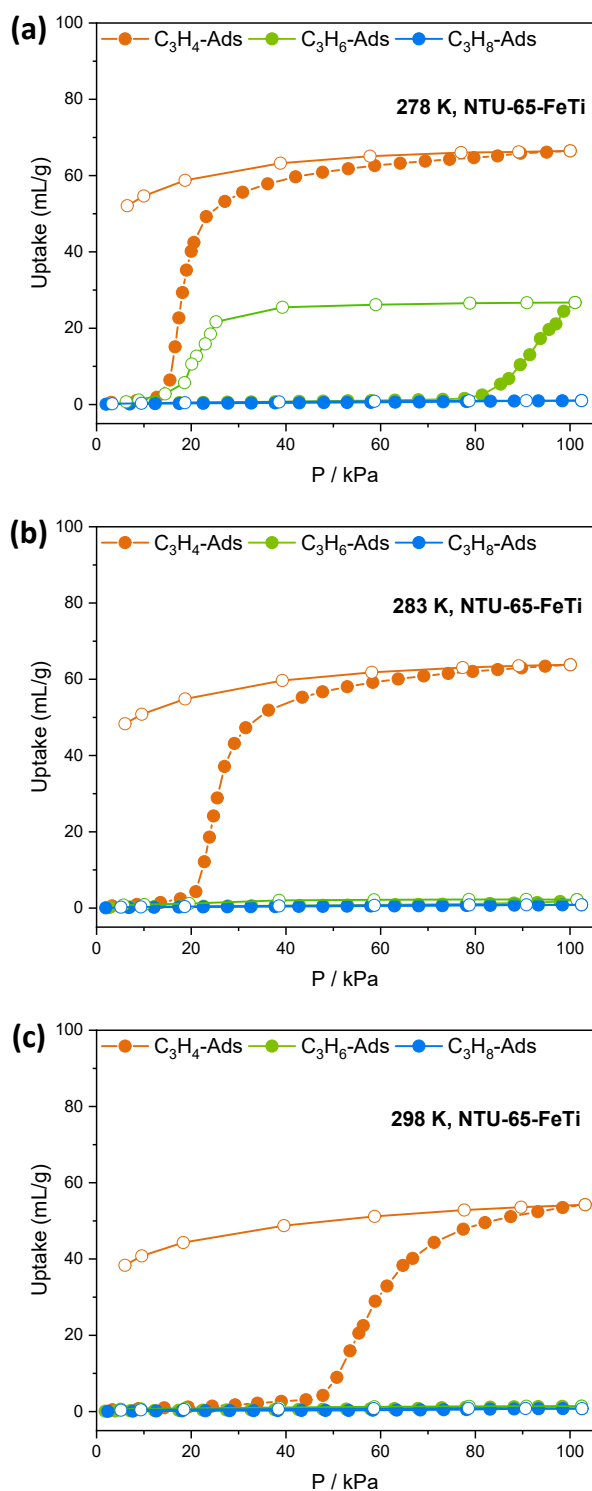


Figure S16. Single-component C_3H_4 , C_3H_6 and C_3H_8 isotherms of **NTU-65-FeTi** at 278 (a), 283 (b), and 298 K (c). Following increased temperature, the gate-opening of C_3H_4 becomes late, while the gate-opening only occurs at the temperature < 278 K toward C_3H_6 . However, C_3H_8 can not open the framework threshold the pressure under these temperatures.

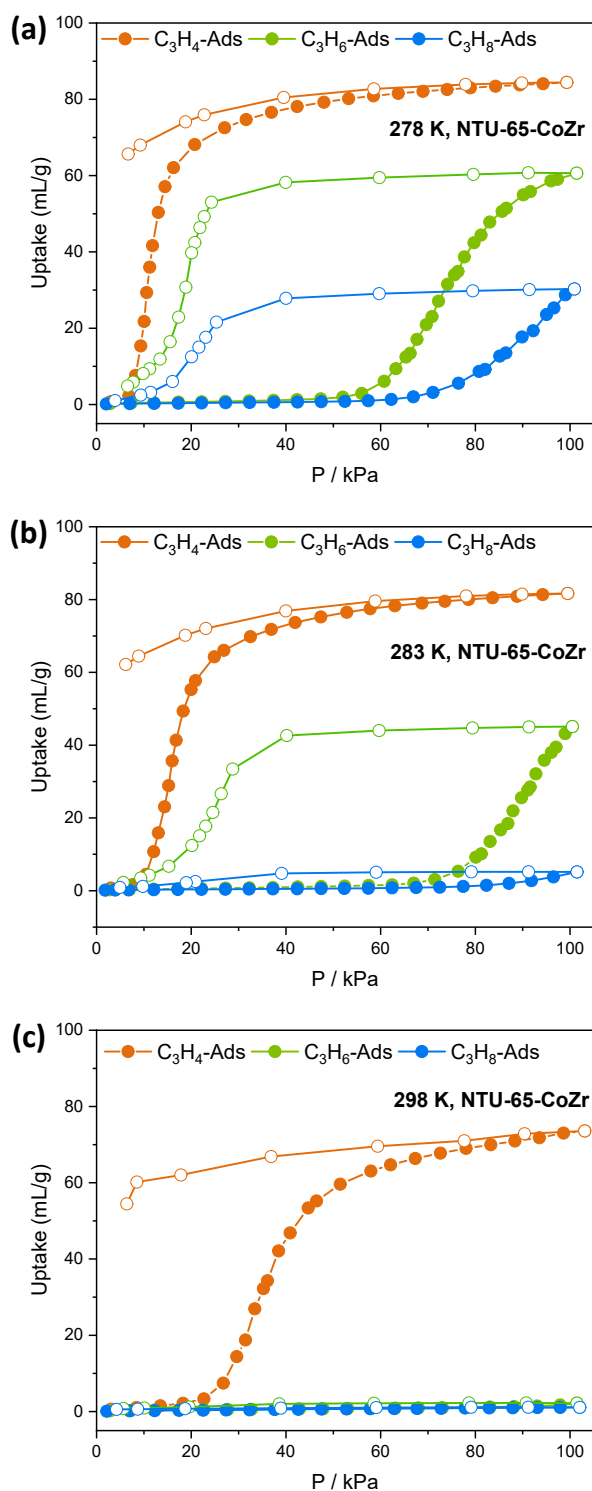


Figure S17. Single-component C_3H_4 , C_3H_6 and C_3H_8 isotherms of **NTU-65-CoZr** at 278 (a), 283 (b), and 298 K (c). Following increased temperature, the gate-opening of C_3H_4 becomes late, while the gate-opening only occurs at the temperature < 283 K toward C_3H_6 . In addition, the gate-opening also occurs toward C_3H_8 when the temperature < 278 K.

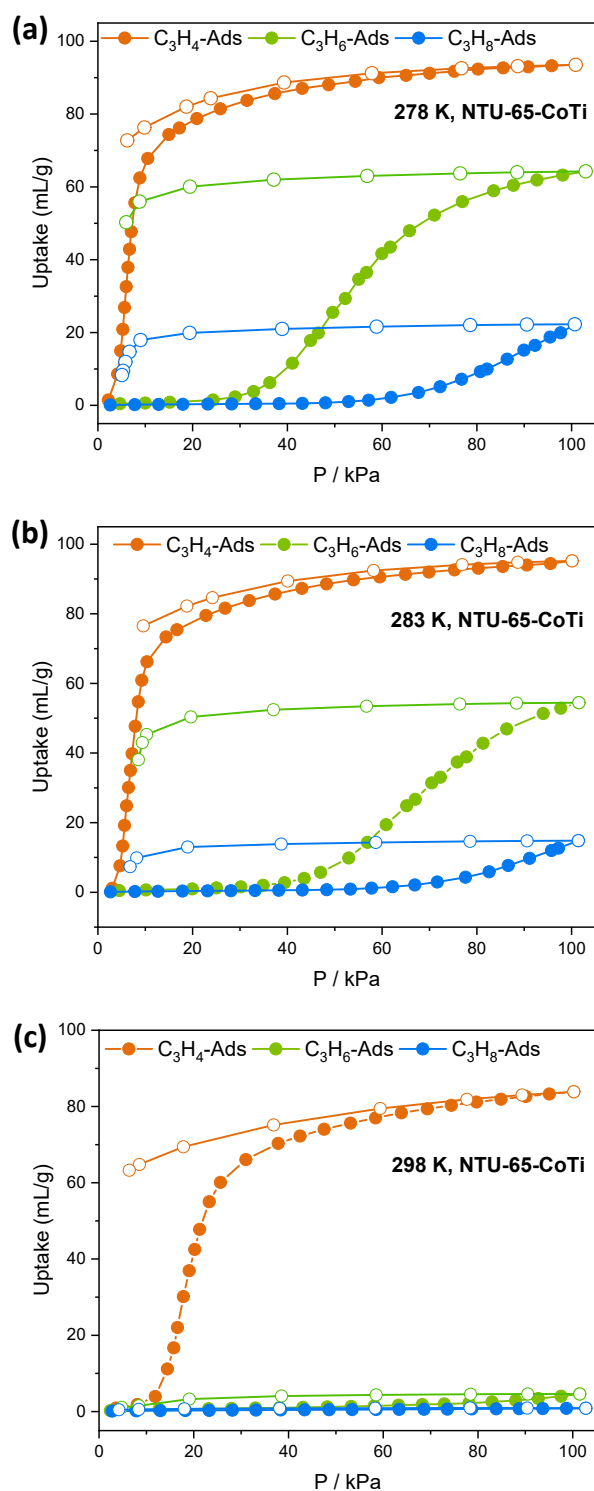


Figure S18. Single-component C_3H_4 , C_3H_6 and C_3H_8 isotherms of **NTU-65-CoTi** at 278 (a), 283 (b), and 298 K (c). Following increased temperature, the gate-opening of C_3H_4 also becomes late, while the gate-opening only occurs at the temperature < 283 K toward C_3H_6 with advanced pressure. In addition, the gate-opening occurs toward C_3H_8 when the temperature < 283 K.

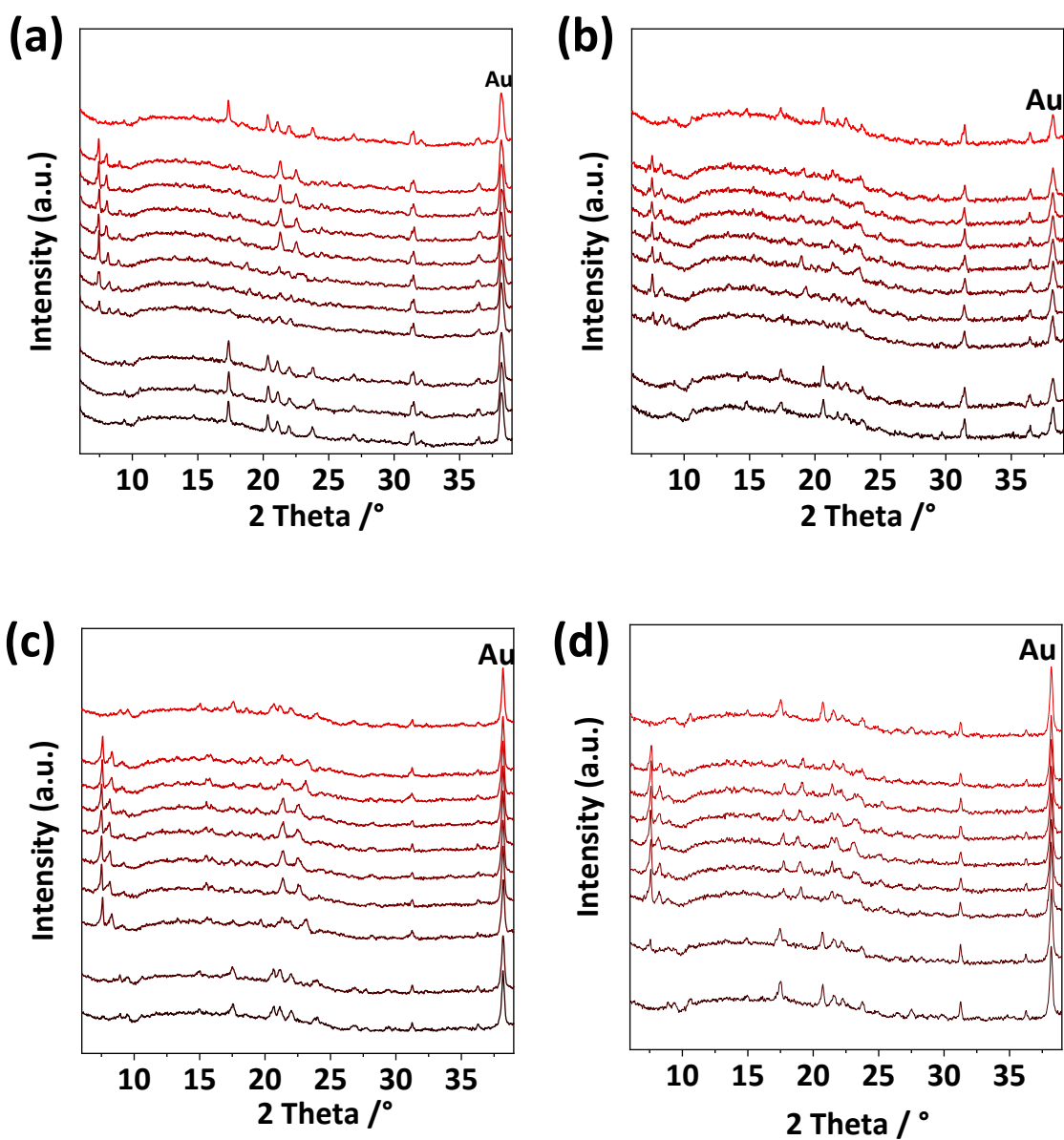


Figure S19. Coincident in-situ PXRD patterns of the four crystals (a: **NTU-65-FeZr**, b: **NTU-65-FeTi**, c: **NTU-65-CoZr**, d: **NTU-65-CoTi**) at given equilibrium pressures during C_3H_4 adsorption and desorption at 273 K. PXRD was collected after 20 min

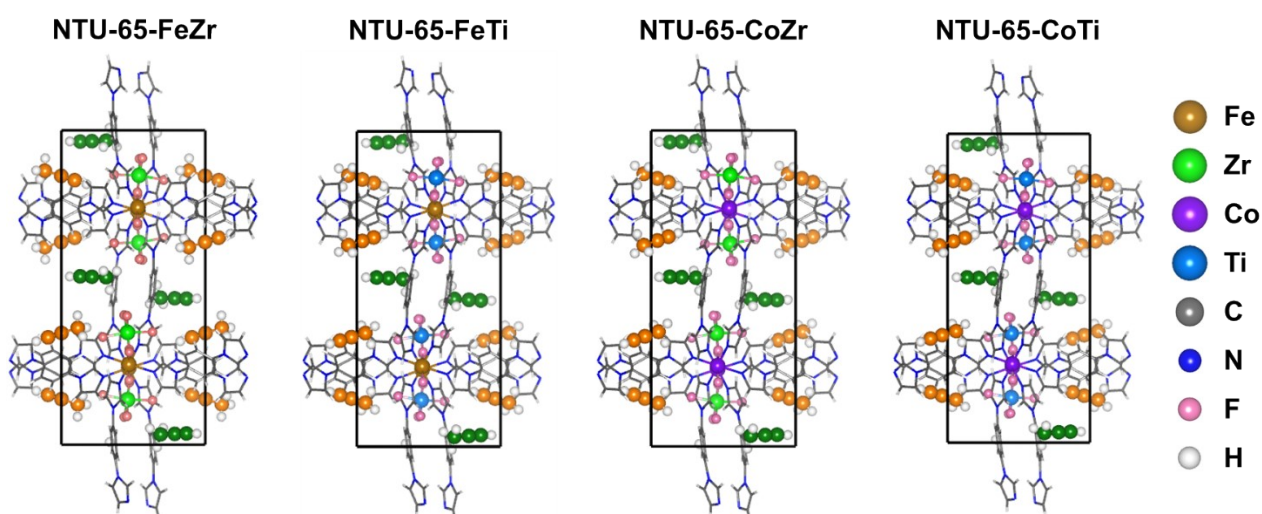


Figure S20. Optimized adsorption structures of C_3H_4 in **NTU-65-series**. The adsorption positions of C_3H_4 were obtained by canonical Monte-Carlo simulation followed by density functional theory calculations. There are two kinds of adsorption sites, each of which contains four symmetrical positions. As a result, a total of eight molecules per unit cell were considered to calculate the binding energy of C_3H_4 with these PCPs. This amount is very similar to the experimental result (once the gate-opening finish: 8.5) for C_3H_4 adsorption in **NTU-65-CoTi**.

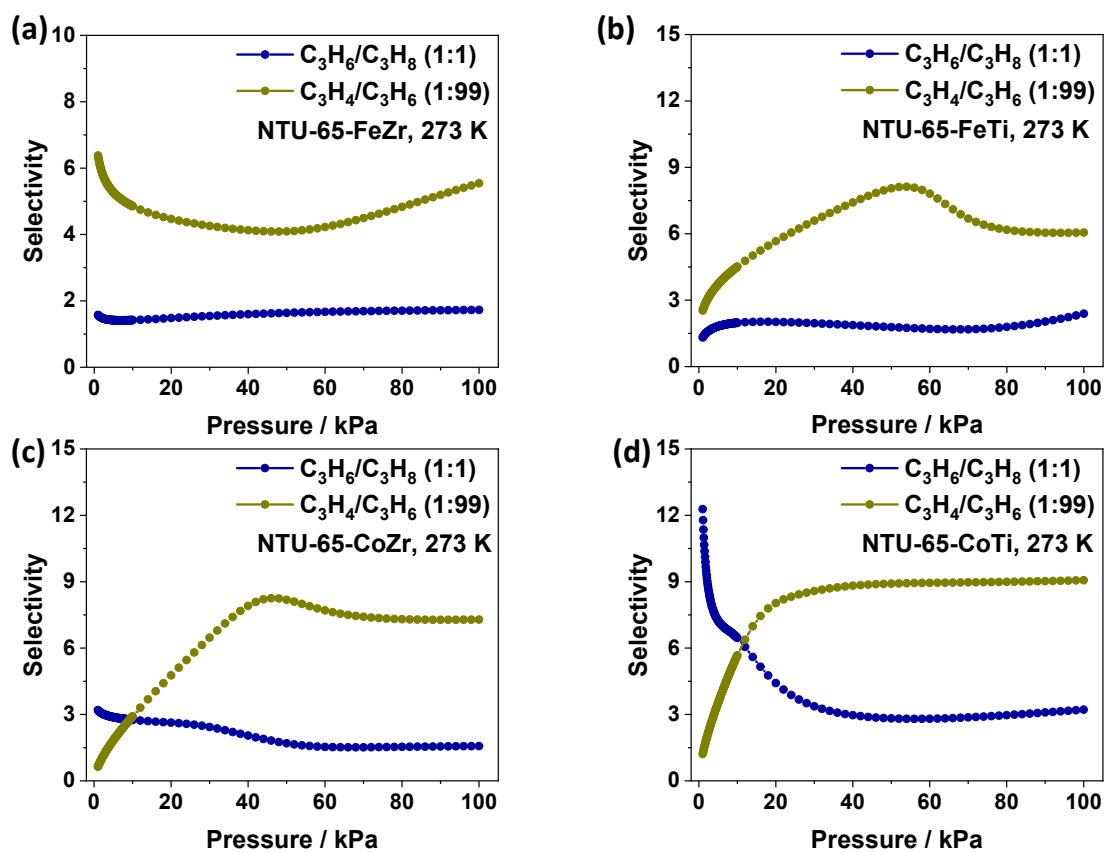


Figure S21. Calculated IAST selectivity for C_3H_4/C_3H_6 mixtures ($v/v = 1/99$) and C_3H_6/C_3H_8 mixtures ($v/v = 1/1$) at 273 K.

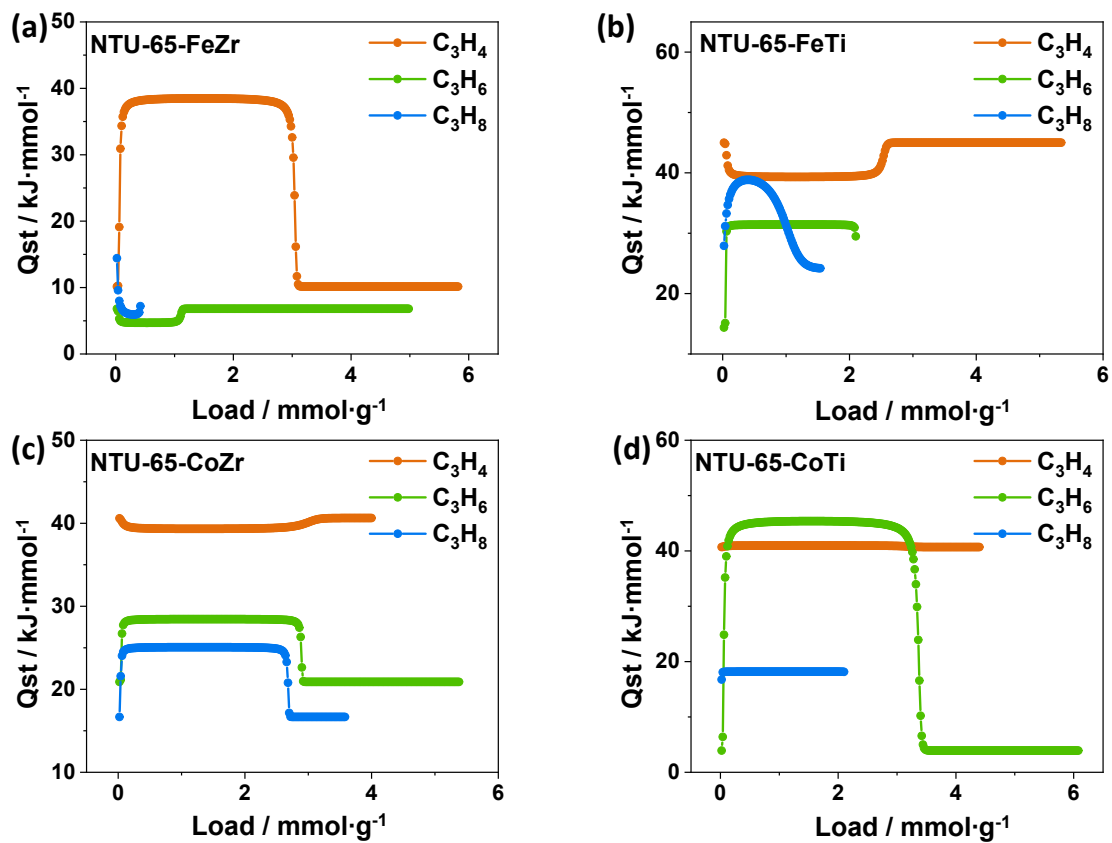


Figure S22. The calculated adsorption heats of C_3H_4 , C_3H_6 and C_3H_8 in NTU-65-series.

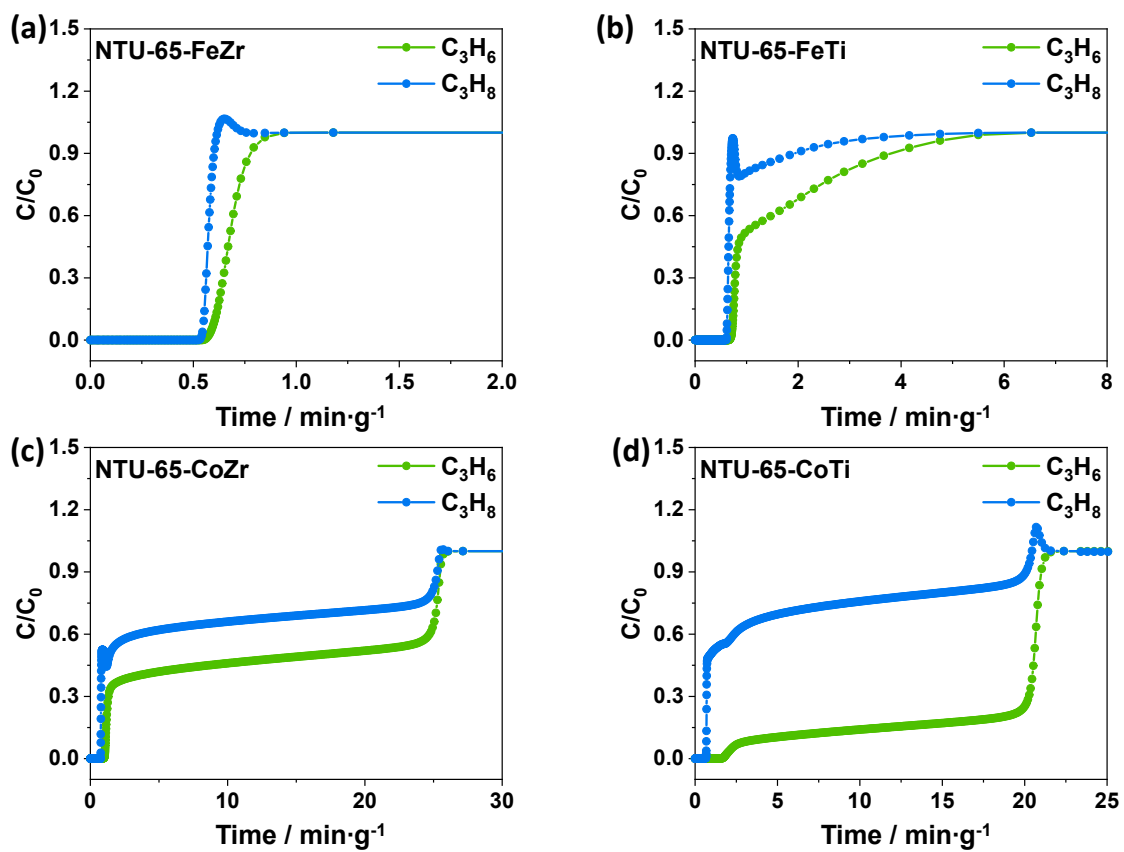


Figure S23. Calculated breakthrough curves for C_3H_6/C_3H_8 mixtures (v/v = 1/1) at 1 bar flowing through a fixed bed of NTU-65-series at 273 K.

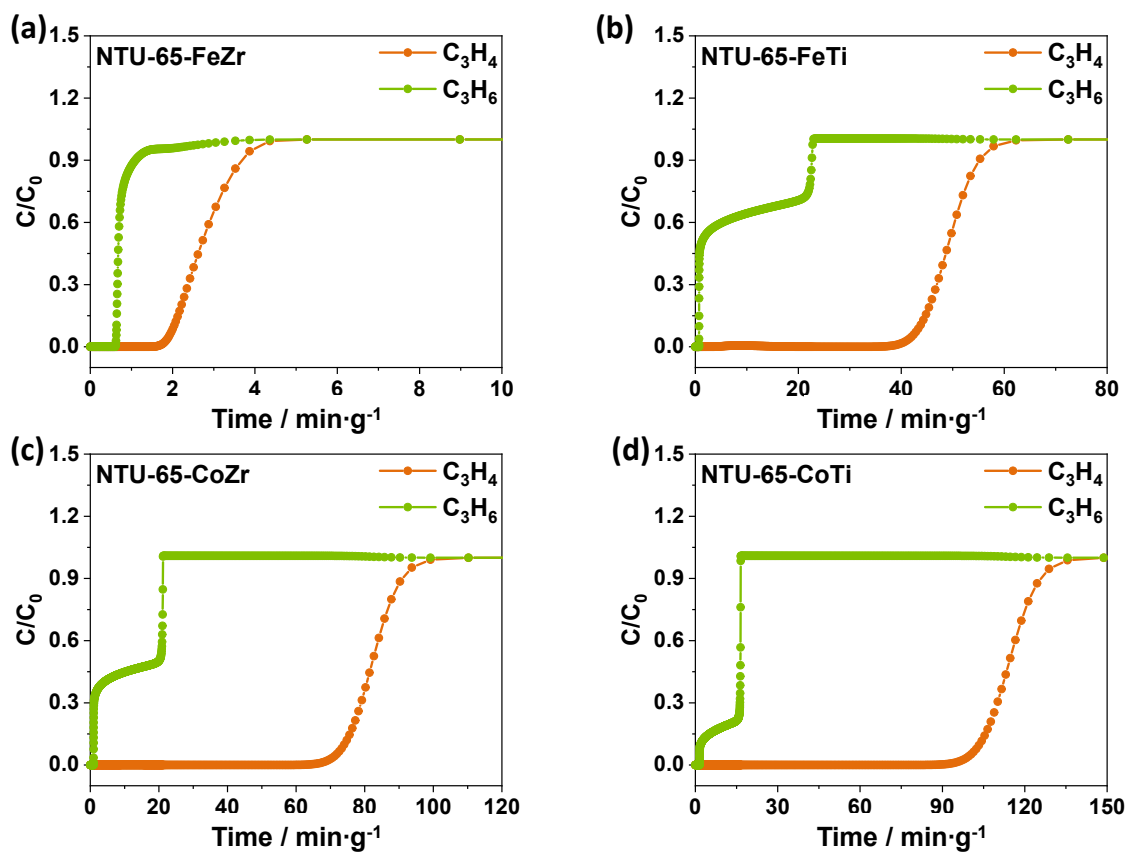


Figure S24. Calculated breakthrough curves for C_3H_4/C_3H_6 mixtures (v/v = 1/99) at 1 bar flowing through a fixed bed of NTU-65-series at 273 K.

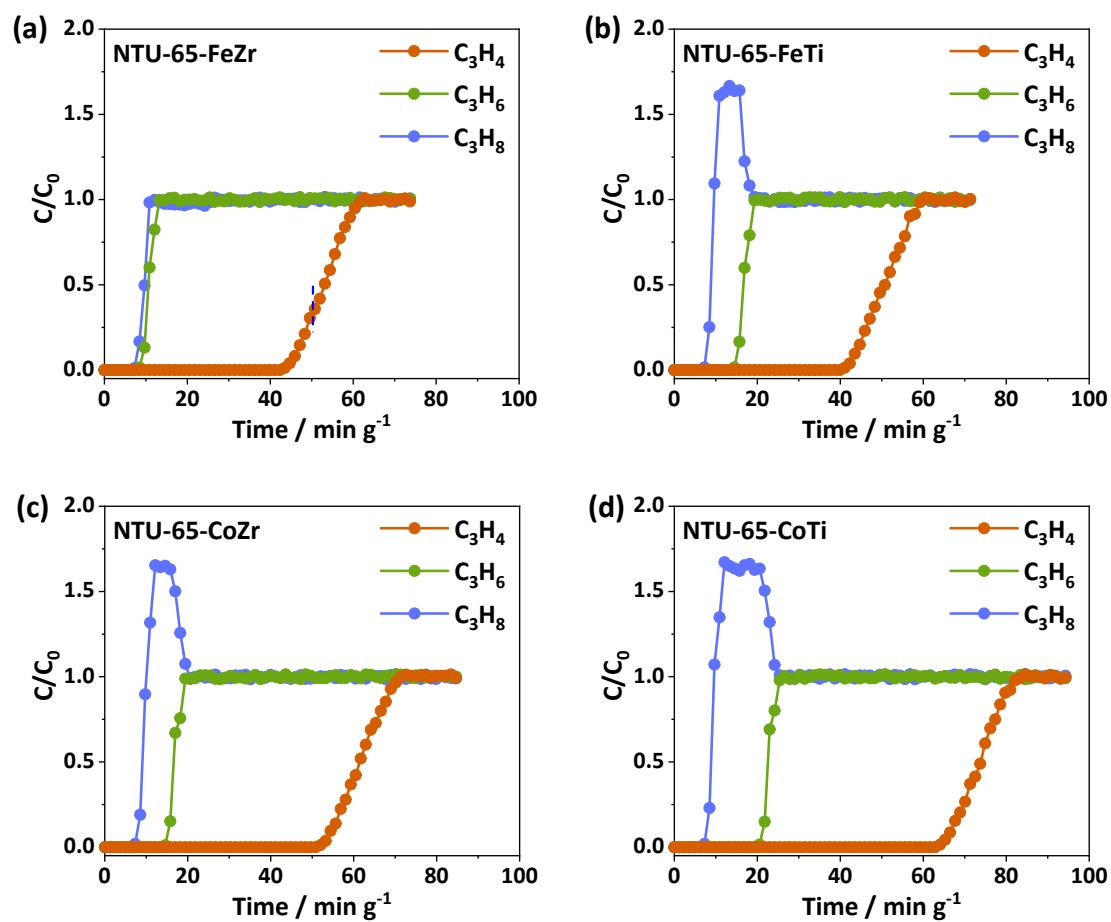


Figure S25. Experimental breakthrough curves of **NTU-65-FeZr** (a), **NTU-65-FeTi** (b), **NTU-65-CoZr** (c) and **NTU-65-CoTi** (d) for $C_3H_4/C_3H_6/C_3H_8$ (0.5/49.75/49.75, v/v/v) separation at 273 K (gas velocity: $5.0 \text{ mL}\cdot\text{min}^{-1}$).

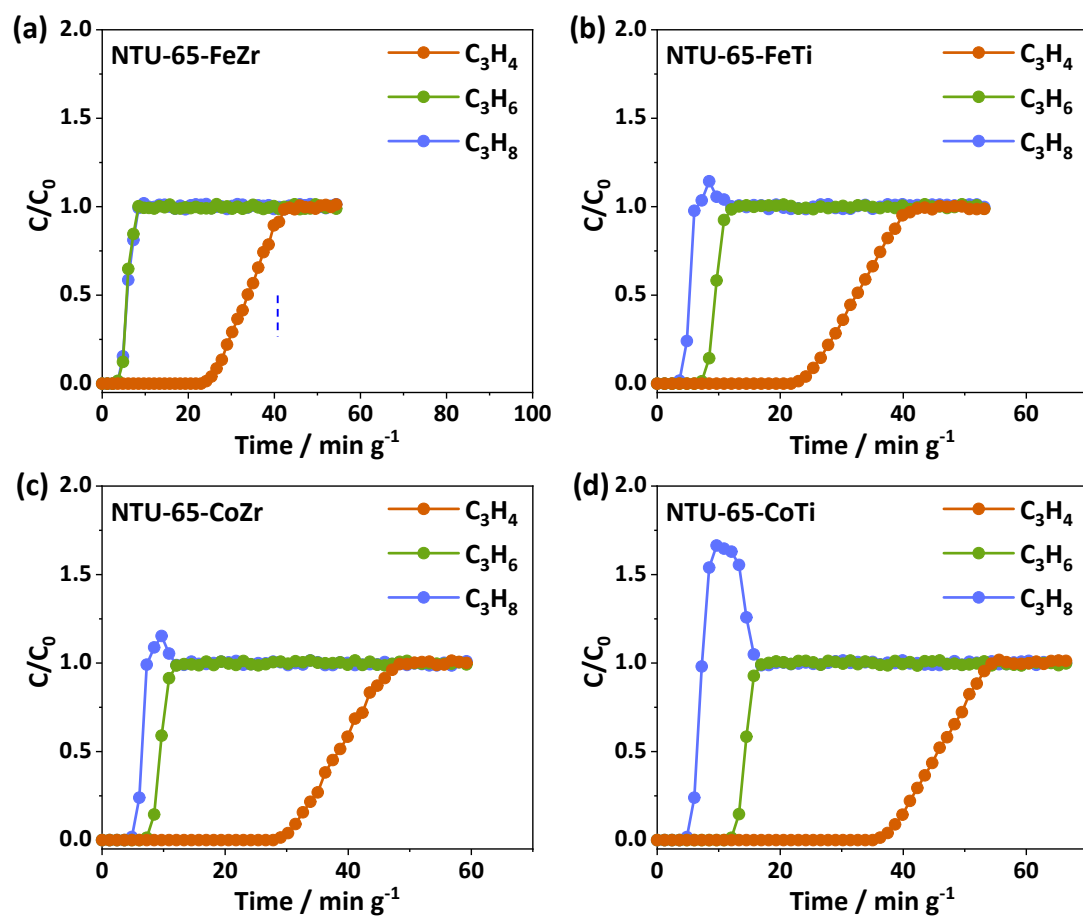


Figure S26. Experimental breakthrough curves of **NTU-65-FeZr** (a), **NTU-65-FeTi** (b), **NTU-65-CoZr** (c) and **NTU-65-CoTi** (d) for $C_3H_4/C_3H_6/C_3H_8$ (0.5/49.75/49.75, v/v/v) separation at 273 K (gas velocity: $10.0 \text{ mL}\cdot\text{min}^{-1}$).

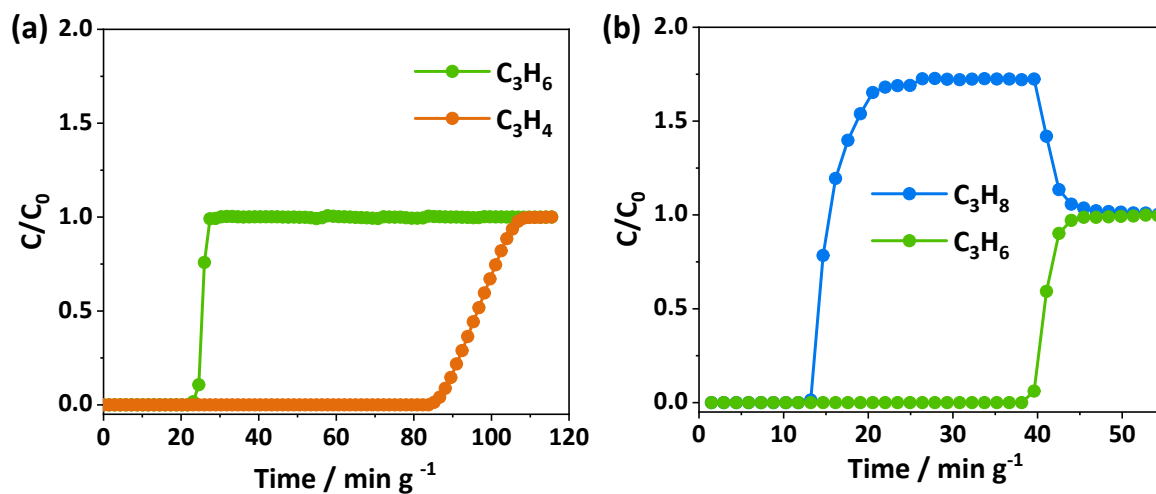


Figure S27. Experimental breakthrough curves of NTU-65-CoTi: (a) $\text{C}_3\text{H}_4/\text{C}_3\text{H}_6$ (1/99, v/v) and (a) $\text{C}_3\text{H}_6/\text{C}_3\text{H}_8$ (1/1, v/v) separation at 273 K (gas velocity: 2.0 mL/min).

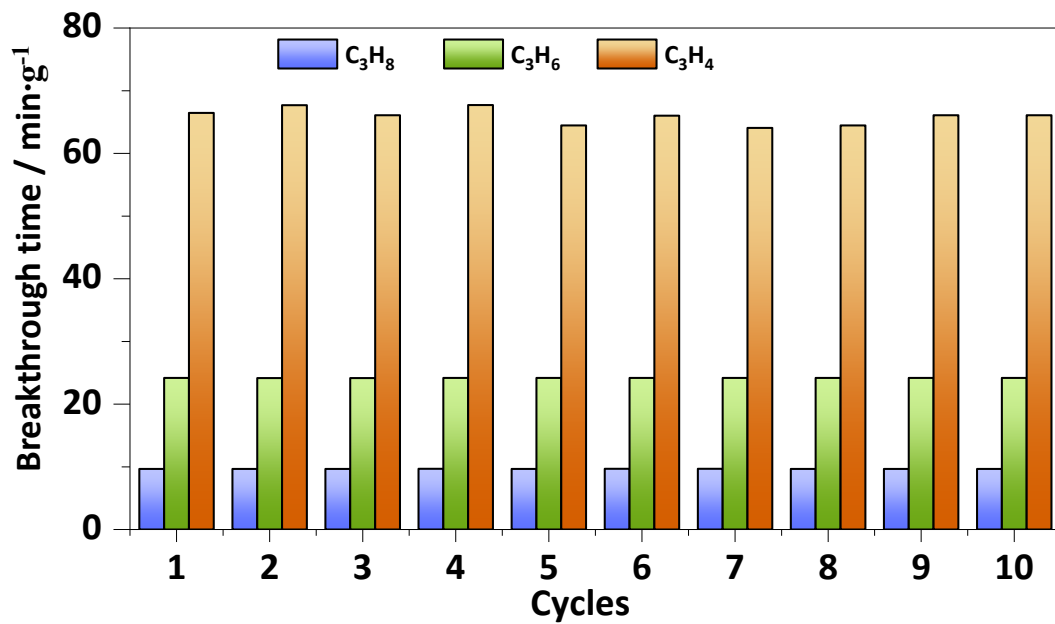
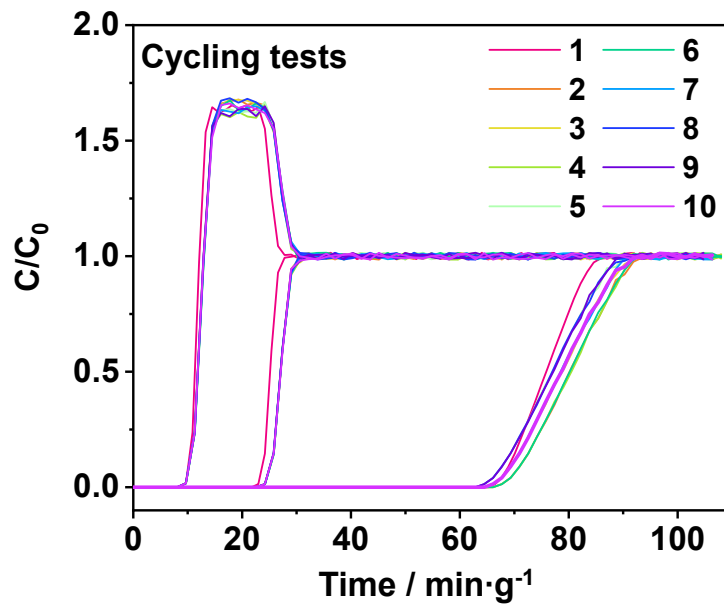


Figure S28. Cycling tests of **NTU-65-CoTi** for the $\text{C}_3\text{H}_4/\text{C}_3\text{H}_6/\text{C}_3\text{H}_8$ mixtures (0.5/49.75/49.75, v/v/v, 5.0 mL/min).

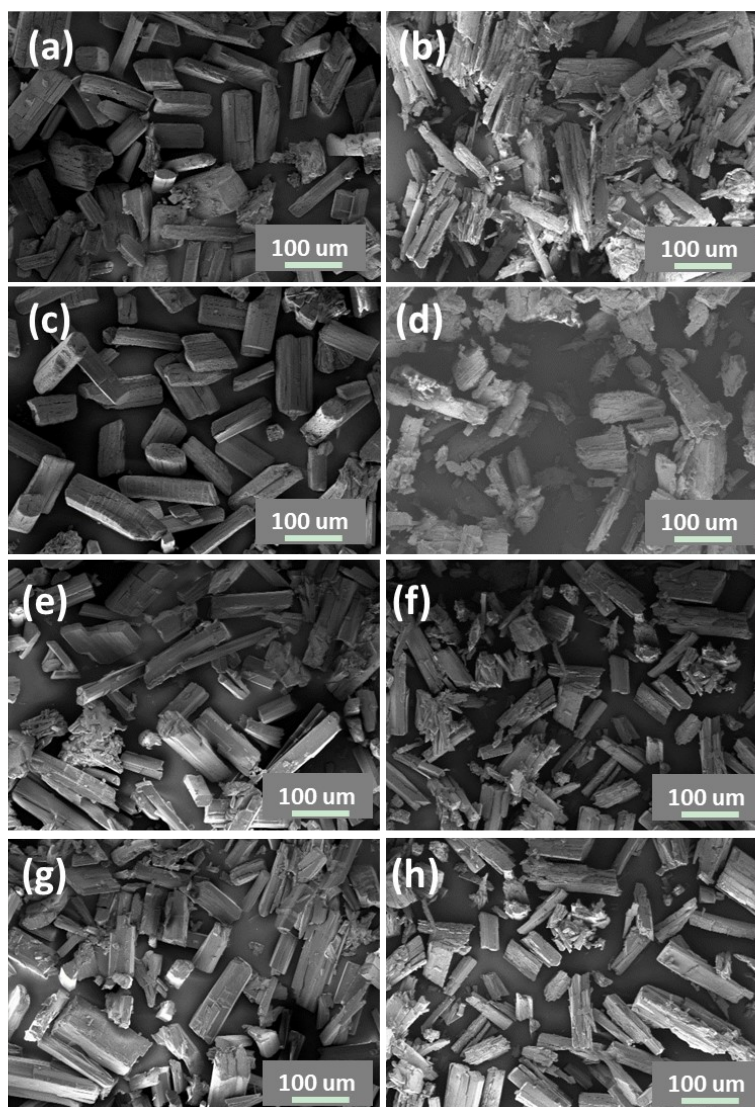


Figure S29. SEM patterns of **NTU-65-FeZr** (a, b), **NTU-65-FeTi** (c, d), **NTU-65-CoZr** (e, f) and **NTU-65-CoTi** (g, h) before activation and after breakthrough measurements.

Table S3. Uptakes ($\text{mL}\cdot\text{g}^{-1}$) of C_3H_4 , C_3H_6 and C_3H_8 in **NTU-65-series** and other benchmark MOFs.

Compounds	Temp. (K)	C_3H_4 uptake		C_3H_6 uptake		C_3H_8 uptake		Uptake ratio of $\text{C}_3\text{H}_4/\text{C}_3\text{H}_6$ (0.1:0.5)	Uptake ratio of $\text{C}_3\text{H}_6/\text{C}_3\text{H}_8$ (0.5:0.5)	Uptake ratio of $\text{C}_3\text{H}_4/\text{C}_3\text{H}_8$ (0.1:0.5)	Ref.
		0.1 bar	1 bar	0.5 bar	1 bar	0.5 bar	1 bar				
Ternary separation											
NTU-65-CoTi	273	73.9	95.9	57.4	75.0	1.6	34.6	1.3	35.9	46.2	This work
NTU-65-CoZr		46.2	87.0	8.6	66.2	1.0	40.4	5.4	8.6	46.2	
NTU-65-FeTi		3.9	69.0	1.3	44.2	0.7	1.4	3.0	1.9	5.6	
NTU-65-FeZr		0.6	74.7	0.7	4.4	0.5	1.0	0.9	1.4	1.2	
$\text{C}_3\text{H}_4/\text{C}_3\text{H}_6$ separation											
UTSA-200	298	73.9	80.2	15.7	26.9	-	-	4.7	-	-	23
ZU-13	298	69.4	86.9	27.2	31.4	-	-	2.6	-	-	24
ELM-12	298	56.9	62.0	26.0	32.0	-	-	2.2	-	-	25
NbOFFIVE-1-Ni	298	38.5	42.3	21.3	27.5	-	-	1.8	-	-	26
SIFSIX-1-Cu		153.4	196.2	121.2	132.2	-	-	1.3	-	-	
SIFSIX-2-Cu-i		65.0	92.5	53.7	59.6	-	-	1.2	-	-	
SIFSIX-3-Zn		47.3	50.6	37.9	42.2	-	-	1.2	-	-	
SIFSIX-3-Ni		61.2	64.6	55.0	61.5	-	-	1.1	-	-	
NKMOF-1-Ni	298	53.8	78.4	38.4	46.0	-	-	1.4	-	-	27
ZU-62	298	67.4	83.0	53.0	60.6	-	-	1.3	-	-	28
Fe-MOF-74	318	149.4	177.9	136.6	148.5	-	-	1.1	-	-	29
SIFSIX-Cu-TPA	298	152.6	188.3	120.8	130.1	-	-	1.3	-	-	30
sql-NbOFFIVE-bpe-Cu-AB	298	53.7	65.1	42.4	47.0	-	-	1.3	-	-	31
GeFSIX-dps-Cu	273	74.6	86.7	1.8	1.8	-	-	41.4	-	-	32
GeFSIX-dps-Zn		49.7	85.1	1.8	1.8	-	-	27.6	-	-	
$\text{C}_3\text{H}_6/\text{C}_3\text{H}_8$ separation											
NTU-85	298	-	-	9.0	10.2	0.02	0.06	-	450	-	33
JUN-3a	273	-	-	65.6	69.4	56.3	58.7	-	1.2	-	34
	303	-	-	51.3	58.6	14.6	48.0	-	3.5	-	
HOF-16a	273	-	-	62.7	68.5	36.9	41.8	-	1.7	-	35
Ni(BDC)(TED) _{0.5}	273	-	-	152.3	160.9	144.7	151.8	-	1.1	-	36
Co-gallate	273	-	-	85.8	96.9	6.6	9.8	-	13.0	-	37
	298	-	-	30.1	40.1	2.8	3.1	-	10.8	-	
CPL-1	273	-	-	28.9	40.8	5.1	6.5	-	5.7	-	38
UTSA-400	298	-	-	38.1	42.3	1.1	1.1	-	34.6	-	39
NKU-FlexMOF-1	273	-	-	72.2	73.6	59.5	61.1	-	1.2	-	40
	298	-	-	69.6	69.9	63.5	65.7	-	1.1	-	
KAUST-7	298	-	-	25.2	31.4	0.5	2.0	-	50.4	-	41
$\text{Co}_2(\text{m-dobdc})$	298	-	-	166.2	170.7	129.5	137.3	-	1.3	-	42
Y-abtc	298	-	-	43.0	44.3	1.4	1.4	-	30.7	-	43
Ni-NP	298	-	-	72.1	79.6	41.2	47.7	-	1.8	-	44
ZJU-75a	296	-	-	64.3	74.1	45.8	52.2	-	1.4	-	45

Note: “-” means no available data.

Table S4. Dual-site Langmuir-Freundlich fits for C₃H₄, C₃H₆ and C₃H₈ in **NTU-65-FeZr**.

	Site A				Site B			
	$\frac{q_{A.sat}}{\text{mol kg}^{-1}}$	$\frac{b_{A,0}}{\text{Pa}^{-\nu_A}}$	$\frac{E_A}{\text{kJ mol}^{-1}}$	ν_A	$\frac{q_{B.sat}}{\text{mol kg}^{-1}}$	$\frac{b_{B,0}}{\text{Pa}^{-\nu_B}}$	$\frac{E_B}{\text{kJ mol}^{-1}}$	ν_B
C ₃ H ₄	3	9.503E-07	6.8	0.67	2.9	2.672E-105	343	8.85
C ₃ H ₆	1	2.225E-51	38.7	8.35	4	2.793E-07	5.1	0.75
C ₃ H ₈	0.4	1.104E-11	8.6	1.6	0.025	3.449E-11	35	0.85

Table S5. Dual-site Langmuir-Freundlich fits for C₃H₄, C₃H₆ and C₃H₈ in **NTU-65-FeTi**.

	Site A				Site B			
	$\frac{q_{A.sat}}{\text{mol kg}^{-1}}$	$\frac{b_{A,0}}{\text{Pa}^{-\nu_A}}$	$\frac{E_A}{\text{kJ mol}^{-1}}$	ν_A	$\frac{q_{B.sat}}{\text{mol kg}^{-1}}$	$\frac{b_{B,0}}{\text{Pa}^{-\nu_B}}$	$\frac{E_B}{\text{kJ mol}^{-1}}$	ν_B
C ₃ H ₄	3	8.557E-15	45	1	2.35	2.693E-103	345	8.8
C ₃ H ₆	2.05	4.991E-135	387	12.3	0.07	1.215E-06	11.5	0.8
C ₃ H ₈	0.7	4.388E-22	65	1.5	0.85	4.621E-08	15	0.62

Table S6. Dual-site Langmuir-Freundlich fits for C₃H₄, C₃H₆ and C₃H₈ in **NTU-65-CoZr**.

	Site A				Site B			
	$\frac{q_{A.sat}}{\text{mol kg}^{-1}}$	$\frac{b_{A,0}}{\text{Pa}^{-\nu_A}}$	$\frac{E_A}{\text{kJ mol}^{-1}}$	ν_A	$\frac{q_{B.sat}}{\text{mol kg}^{-1}}$	$\frac{b_{B,0}}{\text{Pa}^{-\nu_B}}$	$\frac{E_B}{\text{kJ mol}^{-1}}$	ν_B
C ₃ H ₄	1.4	3.538E-20	65	1.6	2.6	3.147E-76	259	6.6
C ₃ H ₆	2.8	3.406E-109	302	10.6	2.6	2.832E-07	11.7	0.56
C ₃ H ₈	2.6	9.609E-85	216	8.6	1	6.420E-07	10	0.6

Table S7. Dual-site Langmuir-Freundlich fits for C₃H₄, C₃H₆ and C₃H₈ in **NTU-65-CoTi**.

	Site A				Site B			
	$\frac{q_{A.sat}}{\text{mol kg}^{-1}}$	$\frac{b_{A,0}}{\text{Pa}^{-\nu_A}}$	$\frac{E_A}{\text{kJ mol}^{-1}}$	ν_A	$\frac{q_{B.sat}}{\text{mol kg}^{-1}}$	$\frac{b_{B,0}}{\text{Pa}^{-\nu_B}}$	$\frac{E_B}{\text{kJ mol}^{-1}}$	ν_B
C ₃ H ₄	1.6	4.130E-18	59	1.45	2.8	1.321E-70	250	6.1
C ₃ H ₆	3.2	3.359E-66	225	4.9	2.9	3.229E-05	2	0.51
C ₃ H ₈	2.1	2.844E-56	120	6.6	0.02	3.360E-07	9.7	1.2

Notation

b	Langmuir-Freundlich constant, $\text{Pa}^{-\nu}$
E	energy parameter, J mol^{-1}
L	length of packed bed adsorber, m
m_{ads}	mass of adsorbent packed in fixed bed, kg
q	component molar loading of species i , mol kg^{-1}
q_{sat}	saturation loading, mol kg^{-1}
Q_0	volumetric flow rate of gas mixture entering fixed bed, $\text{m}^3 \text{s}^{-1}$
Q_{st}	isosteric heat of adsorption, J mol^{-1}
T	absolute temperature, K

Greek letters

ν	Freundlich exponent, dimensionless
-------	------------------------------------

Reference

1. G. M. Sheldrick, A short history of SHELX, *Acta Crystallogr. Sec. A*, 2008, **64**, 112-122.
2. A. L. Spek, *PLATON, A Multipurpose Crystallographic Tool (Utrecht University, 2001)*.
3. P. Vandersluis and A. L. Spek, Bypass - an Effective Method for the Refinement of Crystal-Structures Containing Disordered Solvent Regions, *Acta Crystallogr. Sec. A*, 1990, **46**, 194-201.
4. R. Krishna, The Maxwell-Stefan description of mixture diffusion in nanoporous crystalline materials, *Microporous Mesoporous Mater.*, 2014, **185**, 30-50.
5. R. Krishna, Methodologies for Evaluation of Metal-Organic Frameworks in Separation Applications, *RSC Advances*, 2015, **5**, 52269-52295.
6. R. Krishna, Screening Metal-Organic Frameworks for Mixture Separations in Fixed-Bed Adsorbers using a Combined Selectivity/Capacity Metric, *RSC Advances*, 2017, **7**, 35724-35737.
7. R. Krishna, Methodologies for Screening and Selection of Crystalline Microporous Materials in Mixture Separations, *Sep. Purif. Technol.*, 2018, **194**, 281-300.
8. R. Krishna, Metrics for Evaluation and Screening of Metal-Organic Frameworks for Applications in Mixture Separations, *ACS Omega*, 2020, **5**, 16987-17004.
9. D. Frenkel and B. Smit, Understanding Molecular Simulation: From Algorithms to Applications, *Academic Press, San Diego*, 2002.
10. D. Dubbeldam, S. Calero, D. E. Ellis and R. Q. Snurr, RASPA: molecular simulation software for adsorption and diffusion in flexible nanoporous materials, *Mol. Simul.*, 2016, **42**, 81-101.
11. A. K. Rappe, C. J. Casewit, K. S. Colwell, W. A. Goddard and W. M. Skiff, Uff, a Full Periodic-Table Force-Field for Molecular Mechanics and Molecular-Dynamics Simulations, *J. Am. Chem. Soc.*, 1992, **114**, 10024-10035.
12. T. A. Manz and N. G. Limas, Introducing DDEC6 atomic population analysis: part 1. Charge partitioning theory and methodology, *Rsc Adv*, 2016, **6**, 47771-47801.
13. Y.-L. Peng, C. He, T. Pham, T. Wang, P. Li, R. Krishna, K. A. Forrest, A. Hogan, S. Suepaul, B. Space, M. Fang, Y. Chen, M. J. Zaworotko, J. Li, L. Li, Z. Zhang, P. Cheng and B. Chen, Robust Microporous Metal–Organic Frameworks for Highly Efficient and Simultaneous Removal of Propyne and Propadiene from Propylene, *Angew. Chem. Int. Ed.*, 2019, **58**, 10209-10214.
14. J. P. Perdew, K. Burke and M. Ernzerhof, Generalized gradient approximation made simple, *Phys. Rev. Lett.*, 1996, **77**, 3865-3868.
15. S. Grimme, J. Antony, S. Ehrlich and H. Krieg, A consistent and accurate ab initio parametrization of density functional dispersion correction (DFT-D) for the 94 elements H-Pu, *J. Chem. Phys.*, 2010, **132**, 154104-154122.
16. G. Kresse and J. Furthmuller, Efficiency of ab-initio total energy calculations for metals and semiconductors using a plane-wave basis set, *Comp. Mater. Sci.*, 1996, **6**, 15-50.
17. G. Kresse and J. Furthmuller, Efficient iterative schemes for ab initio total-energy calculations using a plane-wave basis set, *Phys. Rev. B*, 1996, **54**, 11169-11186.
18. P. E. Blochl, Projector Augmented-Wave Method, *Phys. Rev. B*, 1994, **50**, 17953-17979.
19. G. Kresse and D. Joubert, From ultrasoft pseudopotentials to the projector augmented-wave method, *Phys. Rev. B*, 1999, **59**, 1758-1775.
20. S. L. Dudarev, G. A. Botton, S. Y. Savrasov, C. J. Humphreys and A. P. Sutton, Electron-energy-loss spectra and the structural stability of nickel oxide: An LSDA+U study, *Phys. Rev. B*, 1998, **57**, 1505-1509.
21. L. Wang, T. Maxisch and G. Ceder, Oxidation energies of transition metal oxides within the GGA+U framework, *Phys. Rev. B*, 2006, **73**, 195107-195112.
22. V. Stevanovi, S. Lany, X. Zhang and A. Zunger, Correcting density functional theory for accurate predictions of

- compound enthalpies of formation: Fitted elemental-phase reference energies, *Phys. Rev. B*, 2012, 115104-115115.
23. L. B. Li, H. M. Wen, C. H. He, R. B. Lin, R. Krishna, H. Wu, W. Zhou, J. P. Li, B. Li and B. L. Chen, A Metal-Organic Framework with Suitable Pore Size and Specific Functional Sites for the Removal of Trace Propyne from Propylene, *Angew. Chem. Int. Ed.*, 2018, **57**, 15183-15188.
24. L. F. Yang, X. L. Cui, Y. B. Zhang, Q. W. Yang and H. B. Xing, A highly sensitive flexible metal-organic framework sets a new benchmark for separating propyne from propylene, *J. Mater. Chem. A*, 2018, **6**, 24452-24458.
25. L. B. Li, R. B. Lin, R. Krishna, X. Q. Wang, B. Li, H. Wu, J. P. Li, W. Zhou and B. L. Chen, Flexible-Robust Metal-Organic Framework for Efficient Removal of Propyne from Propylene, *J. Am. Chem. Soc.*, 2017, **139**, 7733-7736.
26. L. F. Yang, X. L. Cui, Q. W. Yang, S. H. Qian, H. Wu, Z. B. Bao, Z. G. Zhang, Q. L. Ren, W. Zhou, B. L. Chen and H. B. Xing, A Single-Molecule Propyne Trap: Highly Efficient Removal of Propyne from Propylene with Anion-Pillared Ultramicroporous Materials, *Adv. Mater.*, 2018, **30**, 1705374-1705381.
27. Y. L. Peng, C. H. He, T. Pham, T. Wang, P. F. Li, R. Krishna, K. A. Forrest, A. Hogan, S. Suepaul, B. Space, M. Fang, Y. Chen, M. J. Zaworotko, J. P. Li, L. B. Li, Z. J. Zhang, P. Cheng and B. L. Chen, Robust Microporous Metal-Organic Frameworks for Highly Efficient and Simultaneous Removal of Propyne and Propadiene from Propylene, *Angew. Chem. Int. Ed.*, 2019, **58**, 10209-10214.
28. L. F. Yang, X. L. Cui, Z. Q. Zhang, Q. W. Yang, Z. B. Bao, Q. L. Ren and H. B. Xing, An Asymmetric Anion-Pillared Metal-Organic Framework as a Multisite Adsorbent Enables Simultaneous Removal of Propyne and Propadiene from Propylene, *Angew. Chem. Int. Ed.*, 2018, **57**, 13145-13149.
29. E. D. Bloch, W. L. Queen, R. Krishna, J. M. Zadrozny, C. M. Brown and J. R. Long, Hydrocarbon Separations in a Metal-Organic Framework with Open Iron(II) Coordination Sites, *Science*, 2012, **335**, 1606-1610.
30. Y. J. Jiang, L. Y. Wang, T. A. Yan, J. B. Hu, W. Q. Sun, R. Krishna, D. M. Wang, Z. L. Gu, D. H. Liu, X. L. Cui, H. B. Xing and Y. B. Zhang, Insights into the thermodynamic-kinetic synergistic separation of propyne/propylene in anion pillared cage MOFs with entropy-enthalpy balanced adsorption sites, *Chem. Sci.*, 2023, **14**, 298-309.
31. M.-Y. Gao, A. A. Bezrukov, B.-Q. Song, M. He, S. J. Nikkhah, S.-Q. Wang, N. Kumar, S. Darwish, D. Sensharma, C. Deng, J. Li, L. Liu, R. Krishna, M. Vandichel, S. Yang and M. J. Zaworotko, Highly Productive C₃H₄/C₃H₆ Trace Separation by a Packing Polymorph of a Layered Hybrid Ultramicroporous Material, *J. Am. Chem. Soc.*, 2023, **145**, 11837-11845.
32. T. Ke, Q. Wang, J. Shen, J. Zhou, Z. Bao, Q. Yang and Q. Ren, Molecular Sieving of C-2-C-3 Alkene from Alkyne with Tuned Threshold Pressure in Robust Layered Metal-Organic Frameworks, *Angew. Chem. Int. Ed.*, 2020, **59**, 12725-12730.
33. Q. Dong, Y. Huang, J. Wan, Z. Lu, Z. Wang, C. Gu, J. Duan and J. Bai, Confining Water Nanotubes in a Cu₁₀O₁₃-Based Metal-Organic Framework for Propylene/Propane Separation with Record-High Selectivity, *J. Am. Chem. Soc.*, 2023, **145**, 8043-8051.
34. H. Zeng, M. Xie, T. Wang, R.-J. Wei, X.-J. Xie, Y. Zhao, W. Lu and D. Li, Orthogonal-array dynamic molecular sieving of propylene/propane mixtures, *Nature*, 2021, **595**, 542-548.
35. J. Gao, Y. Cai, X. Qian, P. Liu, H. Wu, W. Zhou, D.-X. Liu, L. Li, R.-B. Lin and B. Chen, A Microporous Hydrogen-Bonded Organic Framework for the Efficient Capture and Purification of Propylene, *Angew. Chem. Int. Ed.*, 2021, **60**, 20400-20406.
36. M. Chang, J. Ren, Y. Wei, J.-X. Wang, Q. Yang, D. Liu and J.-F. Chen, A robust metal-organic framework with guest molecules induced splint-like pore confinement to construct propane-trap for propylene purification, *Sep. Purif. Technol.*, 2021, **279**, 119656.
37. B. Liang, X. Zhang, Y. Xie, R. B. Lin, R. Krishna, H. Cui, Z. Q. Li, Y. S. Shi, H. Wu, W. Zhou and B. L. Chen, An Ultramicroporous Metal-Organic Framework for High Sieving Separation of Propylene from Propane, *J. Am. Chem. Soc.*, 2020, **142**, 17795-17801.
38. Y. Chen, Z. Qiao, D. Lv, C. Duan, X. Sun, H. Wu, R. Shi, Q. Xia and Z. Li, Efficient adsorptive separation of C₃H₆ over

- C₃H₈ on flexible and thermoresponsive CPL-1, *Chem. Eng. J.*, 2017, **328**, 360-367.
39. Y. Xie, Y. S. Shi, E. M. C. Morales, A. El Karch, B. Wang, H. Arman, K. Tan and B. L. Chen, Optimal Binding Affinity for Sieving Separation of Propylene from Propane in an Oxyfluoride Anion-Based Metal-Organic Framework, *J. Am. Chem. Soc.*, 2023, **145**, 2386-2394.
40. M.-H. Yu, B. Space, D. Franz, W. Zhou, C. He, L. Li, R. Krishna, Z. Chang, W. Li, T.-L. Hu and X.-H. Bu, Enhanced Gas Uptake in a Microporous Metal–Organic Framework via a Sorbate Induced-Fit Mechanism, *J. Am. Chem. Soc.*, 2019, **141**, 17703-17712.
41. A. Cadiou, K. Adil, P. M. Bhatt, Y. Belmabkhout and M. Eddaoudi, A metal-organic framework-based splitter for separating propylene from propane, *Science*, 2016, **353**, 137-140.
42. J. E. Bachman, M. T. Kapelewski, D. A. Reed, M. I. Gonzalez and J. R. Long, M₂(m-dobdc) (M = Mn, Fe, Co, Ni) Metal-Organic Frameworks as Highly Selective, High-Capacity Adsorbents for Olefin/Paraffin Separations, *J. Am. Chem. Soc.*, 2017, **139**, 15363-15370.
43. H. Wang, X. Dong, V. Colombo, Q. Wang, Y. Liu, W. Liu, X.-L. Wang, X.-Y. Huang, D. M. Proserpio, A. Sironi, Y. Han and J. Li, Tailor-Made Microporous Metal-Organic Frameworks for the Full Separation of Propane from Propylene Through Selective Size Exclusion, *Adv. Mater.*, 2018, **30**, 1805088.
44. Y. Xie, Y. Shi, H. Cui, R.-B. Lin and B. Chen, Efficient Separation of Propylene from Propane in an Ultramicroporous Cyanide-Based Compound with Open Metal Sites, *Small Struct.*, 2021, **3**, 2100125.
45. D. Liu, J. Y. Pei, X. Zhang, X. W. Gu, H. M. Wen, B. L. Chen, G. D. Qian and B. Li, Scalable Green Synthesis of Robust Ultra-Microporous Hofmann Clathrate Material with Record C₃H₆ Storage Density for Efficient C₃H₆/C₃H₈ Separation, *Angew. Chem. Int. Ed.*, 2023, **62**, e202218590.